

# Workspace of Multi-Fingered Hands Using Monte Carlo Method

Arkadeep Narayan Chaudhury<sup>\*</sup>; Ashitava Ghosal<sup>†</sup>

## Abstract

Multi-fingered hands have the capability of dexterous manipulation of grasped objects and thus significantly increase the capabilities of a robot equipped with multi-fingered hands. Inspired by a multi-jointed human finger and the hand, we propose a six-degree-of-freedom model of a three-fingered robotic hand as a parallel manipulator. Two kinds of contact, namely point contact with friction and rolling without slipping between the finger tips and the grasped object, are considered. The point contact with friction is modeled as a three-degree-of-freedom spherical joint and for rolling without slipping, we use the resultant non-holonomic constraints between the grasped object and the fingers. With realistic limits on the joints in the fingers and dimensions of finger segments, we obtain the well-conditioned dexterous manipulation workspace of the parallel manipulator using a Monte Carlo based method. Additionally, we present two new general results – it is shown that maximum position and orientation workspace is obtained when the cross sectional area of the grasped object is approximately equal to the area of the palm of the hand and when rolling without slipping is ensured the size of the well-conditioned workspace is significantly larger ( $\sim 1.2 - 1.5$  times). We also present representative experiments of manipulation by a human hand show that the experimental results are in reasonable agreement with those obtained from simulations. [DOI: 10.1115/1.4039001]

**Keywords:** Monte Carlo method, multi-fingered hand, well conditioned workspace, hybrid parallel manipulator

## 1 Introduction

The ability of dexterous manipulation has been practiced to perfection by us throughout several thousands of years of evolution ([1]) and therefore it is not surprising that the human hand is the gold standard for design of mechanisms for dexterous manipulation ([2]). With this motivation, the robotics community has been involved in developing multi-fingered hands that can achieve the dexterity, accuracy and load carrying capacity of human hands. Investigation into the topic started in late 1960s with the development of myo-electric devices and subsequently significant advancements have been made in the area till date (for a comprehensive review of the state-of-the-art in this topic till early 2000s, see review paper by [3] and the references contained therein). Some of the early major advances were a robotic hand with elastic fingers ([4]), the Salisbury hand ([5]), the Utah-MIT hand ([6]) and the Styx hand ([7]). Post 2000s, due to availability of better manufacturing techniques, more complex hands like the DLR hand ([8]) and the Shadow hand ([9]) were designed and developed. Several of these hands have large degrees of freedom ( $\geq 20$ ), such as the Utah-MIT hand, Shadow hand, DLR hand, and the RBO hand ([10]) have focused on simulating human like grasping and manipulation of objects with complex shapes. While the anatomically correct testbed (ACT) hand ([11]), focuses on accurately mimicking human hand joint kinematics. It maybe noted that none of these hands have capabilities close to that of a human hand and one of the reasons could be that the human hand, in addition to sophisticated sensing capabilities, has many more links and controlled joints – it is estimated

---

<sup>\*</sup>Graduate Student, Department of Mechanical Engineering, Indian Institute of Science, Bangalore, India. Email: arkadeepc@iisc.ac.in

<sup>†</sup>Corresponding Author, Professor, Department of Mechanical Engineering, Indian Institute of Science, Bangalore, India. Email: asitava@iisc.ac.in

that there are 27 bones controlled by 38 muscles and almost 40 tendons (see [2] and [12]) and the human hand has 27 degrees of freedom.

From modeling and theoretical development viewpoint, the works on obtaining conditions for form closure ([13], conditions for stable grasps in  $\mathbb{R}^3$  ([14]), contact equations between arbitrary smooth bodies ([15] and [16]), grasp criteria and grasp Jacobians ([17]) are some of significant milestones. In another line of research (see, for example, Salisbury [5] and most recently Boras [18]), researchers have explored dexterous manipulation from the context of a parallel manipulator focusing on dexterity, precision of manipulation of a given object in a given workspace by considering a lower degree of freedom ( $\sim 6$ ) approximation of the human hand. In this work we start with the anatomical model of the palm and 3 fingers (index, middle fingers and thumb) of the human hand ([19]) and approximate it as a 6 degree of freedom hybrid parallel manipulator by ruling out certain impossible and unnecessary motions (see [12]). Next, we describe models of contact between the finger tips and an object during manipulation and we consider two models – a point contact with friction modeled as a three-degree-of-freedom spherical joint and a rolling without slipping contact which is also ‘instantaneously’ modeled as a three-degree-of-freedom joint. From the kinematic models, we solve the inverse kinematics problem for the proposed manipulator and obtain the *well conditioned* workspace of the parallel hybrid manipulator using a Monte Carlo method. The main contributions of this work are: **a)** an approach to find the well-conditioned workspace of a human hand inspired 6 degree-of-freedom hybrid parallel manipulator under two possible models of contact between the fingers and the grasped object, **b)** we show that the optimum workspace is obtained when the size of the palm is approximately equal to the size of the grasped object, and the workspace when rolling without slipping is allowed is  $\sim 1.2 - 1.5$  times more than when it is not allowed, and **c)** we perform experiments on dexterous manipulation with a human hand and show that the experimental results are in reasonable agreement with those obtained from numerical simulations and thus validate the algorithm proposed and the methods used in the paper.

The rest of the paper is organized as follows: in section 2 we discuss the Monte Carlo based method used in this work. In section 3 we propose a human hand inspired parallel manipulator model and describe the two models of contact between fingers and objects during manipulation. In section 4 we describe numerical simulation results and experiments and discuss them. Section 5 concludes the work by summarizing the main results.

## 2 Review of Monte Carlo simulation

In this section we present a brief overview of the Monte Carlo method and how it can be used to quantify and obtain a representation of the workspace of a manipulator in  $\mathbb{R}^3$  – for a detailed discussion on the Monte Carlo method, one may refer to any standard textbook of Monte Carlo method such as [20], [21]. The Monte Carlo method has been used by researchers for design and optimization of parallel manipulators (see, for example, [22] and [23] and [24]).

The Monte Carlo method can be used to evaluate integrals of arbitrary functions (vector or scalar function of smooth or non-smooth type) over an arbitrary domain. For the integral

$$\mathcal{I} = \int_{[l,u]^d} \mathcal{F}(\mathbf{X}) \, d\mathbf{x} \quad (1)$$

where  $\mathcal{F}(\cdot)$  is a bounded real valued function over the domain  $[l, u]^d$ , an estimate of  $\mathcal{I}$  can be obtained as  $\widehat{\mathcal{I}}$  as

$$\widehat{\mathcal{I}} = \lim_{n \rightarrow \infty} \frac{1}{n} \sum_{i=1}^n \mathcal{F}(\mathbf{U}_i) \quad (2)$$

Equation (2), involves evaluation of  $\mathcal{F}(\mathbf{U})$  where,  $\mathbf{U} = [u_1, u_2, \dots, u_d]^T$  is a  $1 \times d$  vector taking random values  $u_i \in [l, u] \forall i = 1, 2, \dots, d$ . It can be proved (see, for example, [21], [25]) using the strong law of large numbers<sup>1</sup> that the expression in equation (2), *almost surely*<sup>2</sup> converges to  $\mathcal{J}$ . The volume (area) of a manipulator workspace can be posed as an integration problem in  $\mathbb{R}^3$  ( $\mathbb{R}^2$ ) and we use the Monte Carlo method to evaluate the volume of the workspace of a multi-fingered hand<sup>3</sup>.

## 2.1 Obtaining the well conditioned workspace volume of a parallel manipulator

The workspace of a parallel manipulator depends on the choice of the end-effector. For a chosen end-effector, the workspace is defined as the set of possible values of position and orientation of the end-effector that can be achieved. Typically, the Cartesian co-ordinates  $(x, y, z)$  are used to denote the position and three Euler angle  $(\theta, \phi, \psi)$  can be used to parametrize the orientation. In the Monte Carlo method describe above,  $\mathbf{U}$  is the set  $\{x, y, z, \theta, \phi, \psi\}^T$  and this is denoted by  $\mathbf{X}$ . It may be noted that  $\mathbf{X} \in SE(3)$ .

The function equivalent of  $\mathcal{F}(\mathbf{U})$  in the Monte Carlo method is the *well conditioned* workspace of a parallel manipulator (see section 3.3 for a definition of the well-conditioned workspace). We assume that the well-conditioned workspace  $\mathcal{W}$  ( $\mathcal{W} \in SE(3)$ ) is a collection of a finite number (say  $n$ ) of closed sets in  $SE(3)$  bounded by surfaces  $\mathcal{S}_w^i, \forall i = 1, 2, \dots, n$ . We formulate an *in-out* function  $\mathcal{F}$  for  $\mathcal{S}_w^i$ s which takes input of the position and orientation of the end-effector of the manipulator. This function can be represented as

$$\mathcal{F}(\mathbf{X}) = \begin{cases} 1 & \text{if } \mathbf{X} \in \mathcal{W} \\ 0 & \text{if } \mathbf{X} \notin \mathcal{W} \end{cases} \quad (3)$$

The inclusion (or exclusion) of a given position and orientation of the manipulator,  $\mathbf{X} \in SE(3)$ , is determined by the fact that for a given  $\mathbf{X}$  the inverse kinematics problem has real solutions, the active and passive joint values in the parallel manipulator are within prescribed limits and the manipulator Jacobian is well conditioned. Using algorithm 1 described below, we can obtain  $\widehat{\mathcal{W}}$ , an estimate of the well conditioned workspace  $\mathcal{W}$  of the chosen parallel manipulator. In algorithm 2 below,  $V_s$  is the selected search space in the Cartesian space ( $\mathbb{R}^3$ ) and  $V_a$  is the search space in orientation space ( $SO(3)$ ). The total workspace of the manipulator is a subset of  $V_s \times V_a$  (see [26]).

**Purpose :** To obtain an estimate of the well conditioned workspace

**Input:**  $\mathcal{V}_s \in \mathbb{R}^3$  and  $\mathcal{V}_a \in SO(3)$

**Output:**  $\widehat{\mathcal{W}}$

- 1:  $S = 0, \Phi_k = 0 \forall k, k = 0$
- 2: Choose sample size  $\mathcal{N}_{total}$
- 3: **for**  $k \in \{1, 2, \dots, \mathcal{N}_{total}\}$  **do**
- 4:   Obtain a  $\mathbf{X}_k \in SE(3)$  form a uniformly distributed random PDF in  $\mathcal{V}_s$  and  $\mathcal{V}_a$ .
- 5:   Evaluate  $\Phi_k = \mathcal{F}(\mathbf{X}_k)$ ;
- 6:   **if**  $\Phi_k = 1$  **then**
- 7:      $S = S + \Phi_k$
- 8:   **end if**
- 9:    $k = k + 1$
- 10: **end for**
- 11: Compute  $\widehat{\mathcal{W}} = \frac{S}{\mathcal{N}_{total}} \mathcal{V}_s$

**Algorithm 1:** Algorithm for evaluating the well conditioned workspace of a manipulator.

<sup>1</sup>For a sequence of independent, uniformly distributed real random variables  $\mathbf{X} = \{x_1, x_2, x_3, \dots, x_n\}$  such that  $\langle \mathcal{F}(x_i) \rangle < +\infty$  then  $\lim_{n \rightarrow \infty} \frac{1}{n} \sum_{i=1}^n x_i = \langle \mathbf{X} \rangle$ .

<sup>2</sup>It can be proved that the probability of this convergence is 1.

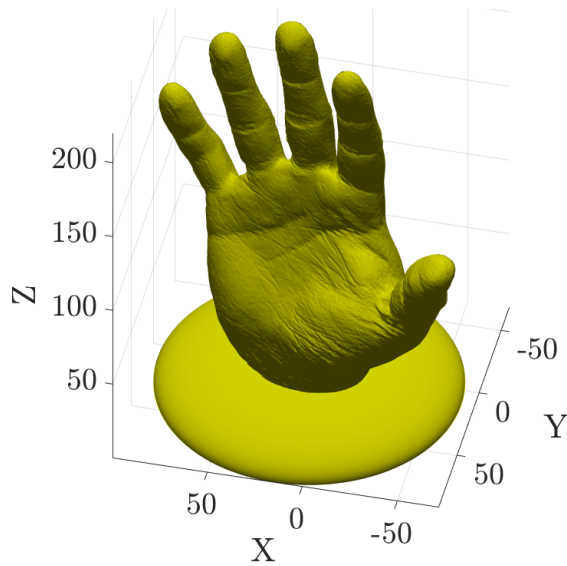
<sup>3</sup>We will also use the Monte Carlo method to obtain the intersection volume of two ellipsoids when rolling contact is assumed.

We present some of the salient features of algorithm 1 which leads to efficient and realistic evaluation of the workspace of a parallel manipulator.

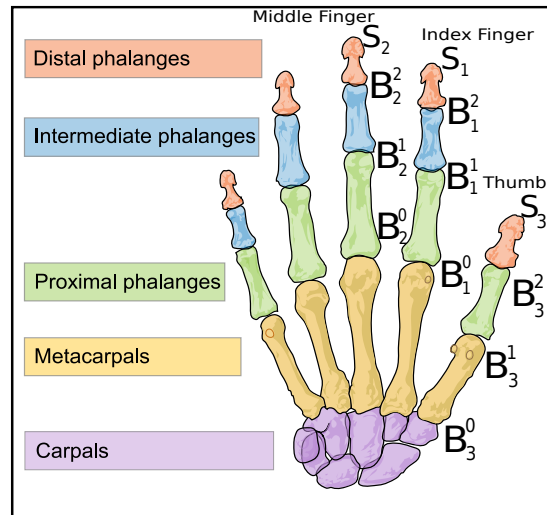
- The `for` loop in line #3–#10 of algorithm 1, can be executed in parallel in a computer implementation. This possibility of parallelization is in fact one of the biggest advantages of the Monte Carlo method and contributes to the exceptional computational performance of the algorithm.
- By choosing a proper distribution  $\mathcal{F}^*(\mathbf{X})$  using information about the underlying process contributing to the success of a simulated sample, a significant improvement can be made in calculation of the estimate of the function over a naive Monte Carlo simulation [21].
- It is well known that typically the inverse kinematics problem of a parallel manipulator is much simpler to solve as compared to the forward kinematics, and we use the inverse kinematics in the formulation. Once the inverse kinematics is solved, we check that the active and passive joint values are within the prescribed limits.
- As shown in Section 3.3, the well-conditioning at a given  $\mathbf{X}$  is based on the condition number of the Jacobian matrices associated with linear and angular velocity of the end-effector. We have used a conservative 1000 as the upper limit of the condition numbers in all our simulations. However, any other upper limit can also be used.

The Monte Carlo simulation as discussed in this section (see also figure 8) classifies a set of position and orientation of the end-effector of a manipulator according to their occurrence in the well conditioned workspace, satisfaction of the inverse kinematics and the prescribed joint limits. The output is a set of points in  $\mathbb{R}^3$  and  $SO(3)$ . For better visualization of the workspace, we obtain the alpha shape (see Edelsbrunner and Mücke [28]) of the cloud of points given by the set  $V_S$  in figure 8 and use standard Delaunay triangulation algorithms [27] to represent the shape of the workspace in 3D, in the form of a triangulated domain.

### 3 Model of a human hand and dexterous manipulation of objects



(a) A 3D scanned model of the human hand



(b) Anatomy of human hand {<https://en.wikipedia.org/wiki/Hand>}

Figure 1: Anatomical and schematic representation of the human hand

Table 1: Sample finger and hand segment lengths (refer figure 3 for symbols)

Hand part	Symbols	Values (mm.)
Index finger	$\{l_{11}, l_{12}, l_{13}\}$	$\{35, 23, 28\}$
Middle finger	$\{l_{21}, l_{22}, l_{23}\}$	$\{41, 22, 28\}$
Thumb	$\{l_{31}, l_{32}, l_{33}\}$	$\{45, 36, 34\}$
Palm	$\{d, h\}$	$\{13, 82\}$

Table 2: Joint notations in figure 3 and maximal permissible motions. The joints with least motion have been selected to remain passive.

Joint center	Joint variable	Type	Value/range
$B_1^0$ and $B_2^0$	$\theta_1$ and $\theta_2$	Active	$0^\circ$ to $90^\circ$
$B_3^0$	$\theta_3$	Active	$-45^\circ$ to $45^\circ$
$B_1^1$ and $B_2^1$	$\phi_1$ and $\phi_2$	Active	$0^\circ$ to $90^\circ$
$B_3^1$	$\phi_3$	Active	$0^\circ$ to $90^\circ$
$B_1^0$ and $B_2^0$	$\psi_1$ and $\psi_2$	Passive	$-15^\circ$ to $15^\circ$
$B_3^2$	$\psi_3$	Passive	$0^\circ$ to $60^\circ$
$B_1^2$ and $B_2^2$	$\gamma_i$ and $\gamma_m$	Fixed	$[0^\circ - 30^\circ]$
$B_3^0$	$\gamma_t$	Fixed	$\gamma_t = 45^\circ$
$S_1, S_2$ and $S_3$	$\{\xi_X^i, \xi_Y^i\}$	Passive	$\pm 45^\circ$

Figure 1a shows a 3D scanned model of a human right hand<sup>4</sup> of a 39 year old Caucasian male. The model of the hand is rendered as an .stl file (see figure 1a). The anatomical details of a typical human hand are shown in figure 1b. For the index and middle fingers, the labels with a suffix 0, i.e.,  $B_1^0$  &  $B_2^0$  represent the *metacarpo-phalangeal joints*,  $B_3^0$  is the trapezium joint between the carpals and metacarpal bone of the thumb. For the index and middle fingers, the joints with suffix one, i.e.,  $B_1^1$  &  $B_2^1$  are the joints between the proximal and intermediate phalanges, for the thumb, the joint  $B_3^1$  indicates the joint between the metacarpal and the proximal phalanx bone. Finally,  $B_1^2$  &  $B_2^2$  indicate the joints between the intermediate and distal phalanges, for the thumb, the joint  $B_3^2$  indicates the joint between proximal and distal phalanx of the thumb. Kinesiological studies (see the work [30] and the references contained therein) have shown that all the joints in the human finger do not equally participate in the prehensile movements of the human hand. For a given grasping task, the motion is generally started from the proximal joints  $B_1^0$ ,  $B_2^0$  &  $B_3^0$  and end in the distal joints  $B_1^2$ ,  $B_2^2$  &  $B_3^2$ , with the proximal joints being active for most of the time [30], the proximal metacarpo-phalangeal joint was active for more than 59% of the motion, the proximal interphalangeal joint was active for 32% of the time and the distal inter-phalangeal joint was active for only 9% of the total time during the execution of a palmer pinching grasping task of a disc from a fully extended position. Based on this reasoning we assume that the proximal joints are actuated and we fix the distal joints of the index and middle fingers  $B_1^2$ ,  $B_2^2$  and make  $B_3^2$  passive. This also makes the model amenable to kinematic analysis since we have 9 joints in the three fingers with six actuated joints which can provide six degrees of freedom to the grasped object<sup>5</sup>. The joints in the fingers have limits and we conservatively choose the joint limit ranges to be at most ranging from  $0^\circ$  to  $90^\circ$ . This is somewhat less to the angles specified by [12], [32], and [33]. Table 1 gives the value of the finger segments of the hand shown in figure 1a measured by using [34]. Table 2 discusses about the joint types and the joint ranges and values of the proposed manipulator.

The possible contacts between the finger tips and the grasped object has been extensively studied in literature (see, for example, [16], [35], [17] and [15]). In this work we study the workspace of the grasped object for two kinds of contact, namely, point contact with friction and point contact with rolling without

<sup>4</sup>The model was obtained by Mr. Georg Weber-Unger Jr. using an Eva<sup>TM</sup> scanner ([29]). The data for figures 1a and 5b are available in public domain and are being used with permission from their respective owners.

<sup>5</sup>A part of this section has been published as [31]. We are reproducing some of it for continuity.

slipping.

### 3.1 Point contact with friction

Following [36] we can express the wrench basis for point contacts with friction as in equation (4) and assuming a Coulomb friction model, the forces transmitted by the contact on the body is given by equation (5). In equation (4),  $I_3$  is the identity matrix of the order 3 and  $\Phi_3$  is the  $3 \times 3$  null matrix and in equation (5),  $\mu$  is the coefficient of friction and  $f_X$ ,  $f_Y$  and  $f_Z$  are the forces transmitted by the point of contact along the  $X$ ,  $Y$  and  $Z$  directions.

$$\mathbb{W} = \begin{bmatrix} I_3 \\ \Phi_3 \end{bmatrix} \quad (4)$$

$$F_o = \mathbb{W} \begin{bmatrix} f_X \\ f_Y \\ f_Z \end{bmatrix}, \quad \sqrt{f_X^2 + f_Y^2} \leq \mu f_Z \quad (5)$$

Since the *ideal* S joint has the same wrench basis as points of contact with friction and it can transmit forces only in the directions given by equation (5), we can replace the contact point by a spherical joint, given that there is negligible motion of the point of contact with respect to the body (see [17] for a similar argument). Figure 2 shows the point of contact modeled as spherical joints with the point S in the figures indicating the center of the joint. Figure 2b shows the interaction of the finger and the object, when the finger tip

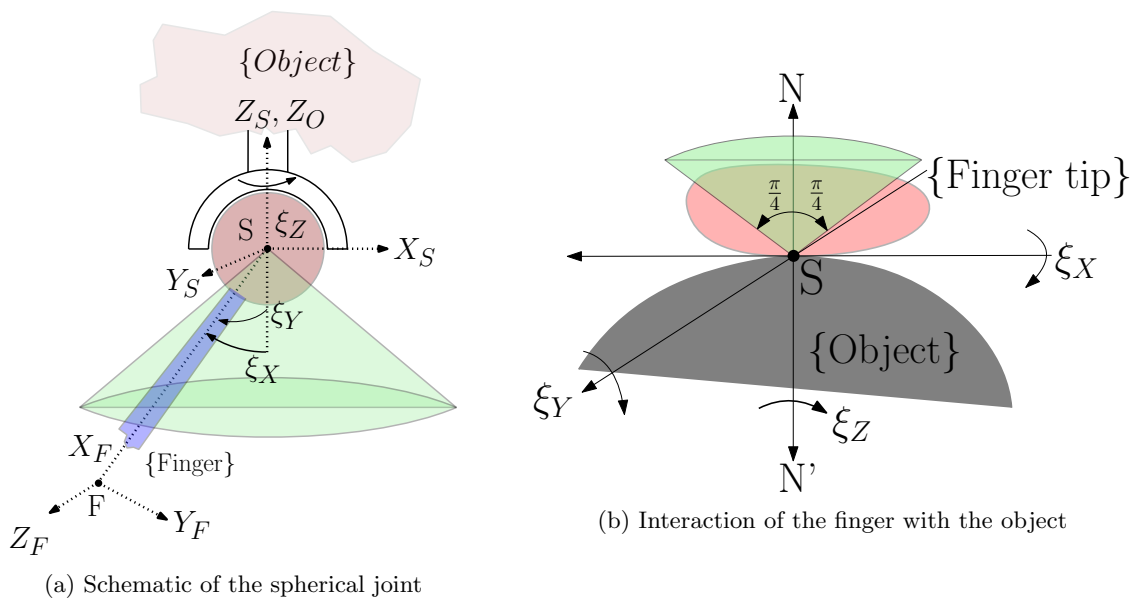


Figure 2: Spherical joint approximation of the finger-tips with object

is approximated as a rigid object with lateral dimensions. The point of contact "S" is assumed to be the center of the S-joint. The green cone in figures 2a and 2b denote the solid angle subtended by the finger about the axis  $Z_S$ . By using the values for  $[R]_O^F$  and  $[R]_O^S$ , the orientations of the finger and the S-joint center with respect to the ground frame, we can obtain the values  $\xi_X$  and  $\xi_Y$  as rotations about  $X_S$  and  $Y_S$ , respectively. With the approximation of the fingertip as a point, the range of the values of  $\xi_X$  and  $\xi_Y$  can be as high as  $\pm 90^\circ$ , however, for fingertips with physical dimensions, such a high value is not possible since, the finger-tip will have a tendency to roll over the object and the point of contact will change. This is shown in figure 2b, where, a smaller permissible range of  $\xi_X$  and  $\xi_Y$  has to be taken. For our simulation, we



a common factor to either sides of the while obtaining the eliminant from equations 8 and 9, using Sylvester's dialytic method. The value of  $\phi_1$  can be obtained symbolically from the dialytic method (see Ghosal [37]) and the value of  $\psi_1$  is obtained symbolically by using terms from the expressions of  $X$  and  $Y$  as

$$\begin{aligned} \psi_1 = \cos^{-1} & [\sin(\pi/4)(X - Y - d)/(\cos(\theta_1 + \phi_1)(l_{12} + l_{13} \cos \gamma_i) \\ & - \sin(\theta_1 + \phi_1) \sin \gamma_i l_{13} + \cos \theta_1 l_{11})] - \pi/4 \end{aligned} \quad (10)$$

The inverse kinematics problem for the middle finger can be solved in a way similar to index finger shown above and the inverse kinematic problem for the thumb is simpler as it can be reduced to a quadratic polynomial. It maybe noted that we have 4 solutions for  $\theta_1$  and the choice of the solutions should take into account the joint limits in table 2. Of the four solutions of  $\theta_1$  obtained from the eliminant, we admit only those which correspond to permissible joint motions (as shown in table 2). Each of the permissible values of  $\theta_1$  are then used to obtain  $\phi_1$  and only a pair of  $\{\theta_1, \phi_1\}$  are admitted, if *both* correspond to permissible joint motions and finally, the admitted values of  $\theta_1$  and  $\phi_1$  are used to find  $\psi_1$ . If and only if  $\theta_i, \phi_i, \psi_i, \forall i = 1, 2, 3$  correspond to permissible joint motions, the solution set is accepted and any violations at any step leads to the rejection of the entire set and also randomly chosen position and orientation of the object. It may also be noted that this check also prevents change in working modes of the manipulator– i.e. flipping of the end effector ( $S_1 S_2 S_3$ ) with respect to the palm ( $B_1^0 B_2^0 B_3^0$ ) as shown in figure 3.

### 3.3 Jacobian matrices and well-conditioning

The position vector of the center of the object in figure 3 is given by,

$${}^O \mathbf{P}_{Obj} = \frac{1}{3} \sum_{i=1}^3 {}^O \mathbf{S}_i \quad (11)$$

and the orientation of the top platform with respect to the base is given by

$${}^O [R]_{Obj} = \left[ \begin{array}{c} \frac{{}^O \mathbf{S}_1 - {}^O \mathbf{S}_2}{{|}^O \mathbf{S}_1 - {}^O \mathbf{S}_2|} \quad \hat{\mathbf{Y}} \quad \frac{({}^O \mathbf{S}_1 - {}^O \mathbf{S}_1) \times ({}^O \mathbf{S}_1 - {}^O \mathbf{S}_3)}{|({}^O \mathbf{S}_1 - {}^O \mathbf{S}_1) \times ({}^O \mathbf{S}_1 - {}^O \mathbf{S}_3)|} \end{array} \right] \quad (12)$$

where  $\hat{\mathbf{Y}}$  is obtained by the cross product of the third and first column of the matrix in equation (12). Differentiating equations (11) and (12) with respect to time we obtain the expressions for the linear and angular velocities of the manipulator.

The 3 constraint equations ensuring that the distance  $\|\mathbf{S}_i - \mathbf{S}_j\|, \{i, j\} \in [1, 2, 3], i \neq j$ , are always constant, may be differentiated to obtain

$$[\mathbf{K}]\{\dot{\theta}, \dot{\phi}\} + [\mathbf{K}^*]\dot{\psi} = 0 \quad (13)$$

where  $\{\theta_i, \phi_i, i = 1, 2, 3\}$  are assumed to be actuated and  $\psi, i = 1, 2, 3$  are assumed to be passive. It is easily seen that  $[\mathbf{K}^*]$  is a square matrix of dimension  $3 \times 3$  and equation (13) can be solved for  $\dot{\psi}$ , given  $\det(\mathbf{K}^*) \neq 0^6$ , and we can obtain

$$\dot{\psi} = -[\mathbf{K}^*]^{-1}[\mathbf{K}]\{\dot{\theta}, \dot{\phi}\} \quad (14)$$

By differentiating the expressions for the linear and angular velocities of the end-effector and partitioning the expression for  $\{\dot{\theta}, \dot{\phi}\}$  and  $\dot{\psi}$ , we have,

$${}^O \mathbf{V}_{Obj} = [\mathbf{J}_V]\{\dot{\theta}, \dot{\phi}\} + [\mathbf{J}_V^*]\dot{\psi} \quad (15)$$

$${}^O \boldsymbol{\omega}_{Obj} = [\mathbf{J}_\omega]\{\dot{\theta}, \dot{\phi}\} + [\mathbf{J}_\omega^*]\dot{\psi} \quad (16)$$

<sup>6</sup>In the simulation, it was ensured that  $\det(\mathbf{K}^*) \neq 0$  and the condition number of  $\mathbf{K}^*$  was  $\leq 10^4$  at all points inside the obtained workspace.

Following [38] and using equations (13), (15) and (16) we define the equivalent Jacobian matrices for both linear and angular velocity parts as

$$\mathbf{J}_{eqv}^V = (\mathbf{J}_V - \mathbf{J}_V^*[\mathbf{K}^*]^{-1}[\mathbf{K}]) \quad (17)$$

$$\mathbf{J}_{eqv}^\omega = (\mathbf{J}_\omega - \mathbf{J}_\omega^*[\mathbf{K}^*]^{-1}[\mathbf{K}]) \quad (18)$$

The equivalent, dimensionless condition number of Jacobian for the manipulator, undergoing both linear and angular motions are given as  $\kappa_V$  and  $\kappa_\omega$  for  $\mathbf{J}_{eqv}^V$  and  $\mathbf{J}_{eqv}^\omega$ , respectively where we find the 2-Norm condition number of a matrix  $\mathbf{A}$  as  $\kappa_A = \|\mathbf{A}\|_2 \|\mathbf{A}^{-1}\|_2$ . To ensure that a given configuration of the end effector is well conditioned we ensure that both the condition numbers are

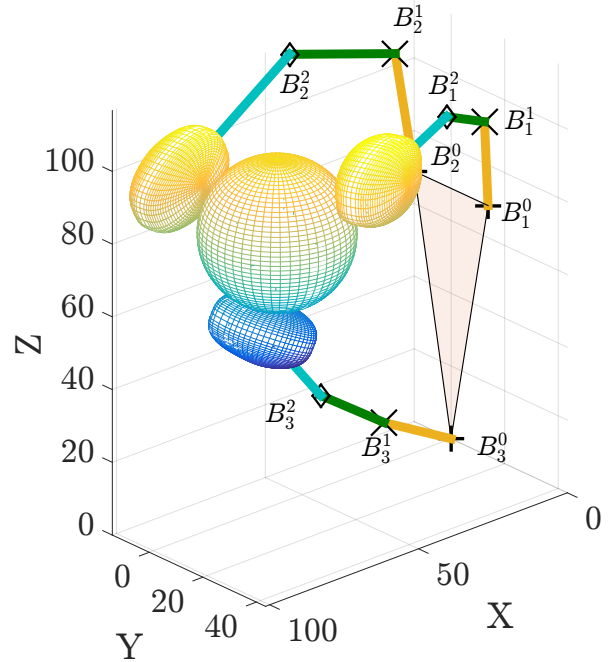
$$\max\{\kappa_V, \kappa_\omega\} \leq \kappa^* \quad (19)$$

In our simulations, we ensure that  $\kappa^* \leq 1000$ . This gives a conservative workspace and a higher value of  $\kappa^*$  can be shown to give a larger well conditioned workspace.

### 3.4 Point contact with rolling without slipping



(a) Human hand manipulating a ball



(b) Snapshot of the computer simulation of the scenario shown in figure 4a

Figure 4: Dexterous manipulation in practice and simulation snapshot

Majority of dexterous manipulation tasks undertaken by our hands involve rolling and sliding type of contact between the hand and object (see [15] for more details). The rolling type of contacts between the fingertips and the object during dexterous manipulation has been widely studied (see for example the pioneering works by [15], [17] and [16] and the references contained therein) and most of these approaches are based around the definition of a quantity called the *grasp Jacobian* or the *grasp map*. In this work, we assume that the grasped object can roll without slipping and we use the contact equations developed by [15] (see appendix A for the equations modeling the contact between the finger and the grasped object). In this

case too, it can be shown that the contact *instantaneously* allows three relative degrees of freedom. The main difference with the spherical joint model is that the constraints are non-holonomic, i.e., they restricts the space of velocities and not the translation and orientation of the grasped object. In order to model the rolling without slip contact, we need a surface model of the finger and the grasped object. The grasped object is assumed to be a sphere and the well-known parametric equations of a sphere is used. For the finger, we model the finger tips as super-ellipsoids and this is discussed next.

### 3.4.1 Fitting super-ellipsoids to cloud of points in $\mathbb{R}^3$

Super ellipsoids are an extension of ellipsoids and have been used for solid modeling in diverse fields such as for modeling and representation of medical data ([39]), high fidelity representation of scanned objects ([40]) and as objects for developing obstacle avoidance algorithms ([41]). The main reason behind it's widespread use is the availability of precise closed form expressions for *almost* all geometrical properties like moments of inertia about arbitrary axes, mass and surface properties like tangents and normals (see [42] for a more complete description). In this work, we use an efficient method based on the works by [40] and further improvements on it by [39] to fit super-ellipsoids to a cloud of points in  $\mathbb{R}^3$ . The goal is to obtain a more accurate approximation of the geometry of human fingertips over normal ellipsoids used by previous researchers (see e.g. [35] and similar works for more details).

Equations (20) to (22) are the parametric expressions that map an arbitrary surface with parameters  $A$ ,  $B$  and  $C$  having dimensions of length and dimensionless exponents  $e$  and  $n$  from  $\{u, v\} \in \mathbb{R}^2 \rightarrow \{x, y, z\} \in \mathbb{R}^3$ . The sign function is abbreviated as "sgn" in equations (20) to (22).

$$x(u, v) = A \operatorname{sgn}(\cos(v)) (|\cos(v)|)^n \operatorname{sgn}(\cos(u)) (|\cos(u)|)^e \quad (20)$$

$$y(u, v) = B \operatorname{sgn}(\cos(v)) (|\cos(v)|)^n \operatorname{sgn}(\sin(u)) (|\sin(u)|)^e \quad (21)$$

$$z(u, v) = C \operatorname{sgn}(\cos(v)) (|\cos(v)|)^n \quad (22)$$

The expression in equation (23) classifies whether a point is in, on or outside the surface expressed by equations (20) to (22) by assuming negative, zero and a positive values respectively.

$$\mathcal{F}(x, y, z) = \left( \left( \left( \frac{x}{A} \right)^{2e-1} + \left( \frac{y}{B} \right)^{2e-1} \right)^{\frac{e}{n}} + \left( \frac{z}{C} \right)^{2n-1} \right)^{\frac{n}{2}} \quad (23)$$

For fitting a superquadric to a cloud of  $n$  points contained in the matrix  $\mathbf{P}$ ,  $\mathbf{P} \in \mathbb{R}^{n \times 3}$  we formulate the following optimization problem given in equation (24). In equation (24), the elements of  $\bar{\mathbf{x}}$  are the coordinates for the center of the super ellipsoid, the elements  $\bar{\Theta}$  are the Euler angles specifying the orientation of the fitted ellipsoid,  $\mathbf{a} = \{A, B, C\}$  and  $\mathbf{p} = \{e, n\}$ .

$$\underset{\bar{\mathbf{x}}, \bar{\Theta}, \mathbf{a}, \mathbf{p}}{\operatorname{Min}} \sum_{i=1}^N \sqrt{ABC} (\mathcal{F}(\mathbf{X}^r, \bar{\Theta}, \mathbf{a}, \mathbf{p}) - 1)^2 \quad (24)$$

In equation (24), the *in-out* function  $F$  from equation (23) is used with the cloud of points  $\mathbf{P}$  transformed to the original coordinate about which equations (20) to (22) are defined. An initial guess about the position and orientation of the cloud of points may be given as follows. The value of  $\bar{\mathbf{x}}$  in equation (25) may be given as the average of the respective coordinates of the points in  $\mathbf{P}$ , i.e.,  $\bar{\mathbf{x}} = \left\{ \frac{1}{n} \sum_{i=1}^n x_i, \frac{1}{n} \sum_{i=1}^n y_i, \frac{1}{n} \sum_{i=1}^n z_i \right\}$ .

$$\left\{ \begin{array}{c} \mathbf{X}^r \\ 1 \end{array} \right\} = [T]_{O}^P \left\{ \begin{array}{c} x_i \\ y_i \\ z_i \\ 1 \end{array} \right\} = \left[ \begin{array}{cc} [R]_{O}^P & \bar{\mathbf{x}} \\ 0 & 1 \end{array} \right] \left\{ \begin{array}{c} x_i \\ y_i \\ z_i \\ 1 \end{array} \right\} \quad (25)$$

In equation (25),  $[R]_O^P$  may be represented as the matrix which diagonalizes the total moment matrix  $M$  of the cloud of points  $\mathbf{P}$  (see equation (26)) to  $M_0$  in the operation  $M_0 = R^{-1}MR = R^TMR$ . In equation (26)  $\tilde{x}_i = (x_i - \bar{x})$ ,  $\tilde{y}_i = (y_i - \bar{y})$  and  $\tilde{z}_i = (z_i - \bar{z})$ .

$$M = \frac{1}{n} \sum_{i=1}^n \begin{bmatrix} \tilde{y}_i^2 + \tilde{z}_i^2 & -\tilde{x}_i\tilde{y}_i & -\tilde{z}_i\tilde{x}_i \\ -\tilde{x}_i\tilde{y}_i & \tilde{x}_i^2 + \tilde{z}_i^2 & -\tilde{y}_i\tilde{z}_i \\ -\tilde{z}_i\tilde{x}_i & -\tilde{y}_i\tilde{z}_i & \tilde{x}_i^2 + \tilde{y}_i^2 \end{bmatrix} \quad (26)$$

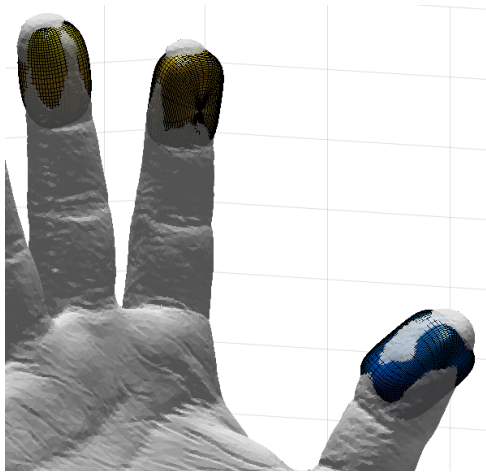
The goodness of the fit, according to [43], may be measured by total value of the first order approximation of the distances of the points in  $\mathbf{P}$  from the fitted surface  $\mathcal{S}$  as given in equation (27).

$$d_S = \sum_{i=1}^n \left( \frac{|\mathcal{F}(x_i, y_i, z_i, \mathbf{a}, \mathbf{p}) - 1|}{\|\nabla \mathcal{F}\|_{\{x_i, y_i, z_i\}}} \right)^2 \quad (27)$$

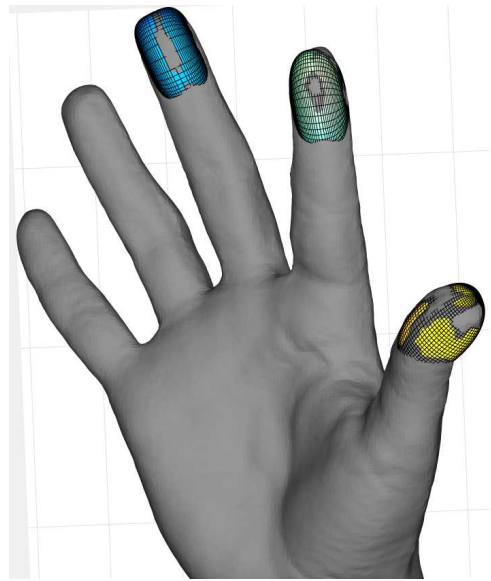
For the hand model shown in figure 1a, from 296,358 vertexes and 98,786 triangular facets available in the raw data (see figure 1a) we pick 40 points from each of the middle finger, index finger and the thumb tips. The unconstrained optimization problem given in equation (24) is quadratic in nature and can be solved using the *Levenberg-Marquardt* method (see [44] for more details). The numerical results for the fit are given in table 3. The plotted results of the same are shown in figure 5.

Table 3: Parameters of the super-ellipsoids fitted to the finger-tips in figure 5a.

Finger	$\mathcal{S} = \{A, B, C, e, n\}$	$d_S$
Index	{14.98, 9.83, 8.33, 1.14, 0.67}	36.23
Middle	{14.99, 7.94, 9.80, 0.72, 0.5}	52.65
Thumb	{11.78, 9.12, 15.0, 0.58, 0.62}	42.8



(a) Superellipsoid approximation of a male subject's hand



(b) Superellipsoid approximation of a female subject's hand

Figure 5: Superellipsoid approximations of human finger-tips. The approximations for the female subject are better due to the higher resolution of the available 3D scan.

### 3.4.2 Collision detection of two super-ellipsoids in $SE(3)$

In the model with the S joints, it is reasonable not to consider the collision between the fingers. In the super-ellipsoid model, the fingers have finite size and to obtain realistic workspace of the multi-fingered hand, it is essential to model the collision and intersection between the super-ellipsoids as this reduces the total workspace. Collision detection and interaction between moving rigid bodies is a generic problem frequently encountered in various fields like robotics (see e.g. [45]), computer aided design(CAD), computer vision (see e.g. [46]) and discrete element method (DEM) simulations (see e.g. [47]). In this work, we use a Monte Carlo based *probabilistic* algorithm to obtain the *intersection volume* of two arbitrarily oriented super-ellipsoids in the 3D space. The intersection volume  $\mathcal{I}(\mathcal{S}_1, \mathcal{S}_2)$  of the two closed solids  $\mathcal{S}_1$  and  $\mathcal{S}_2$  can be obtained using the algorithm 2 given below.

**Purpose :** To obtain an estimate of  $\mathcal{I}(\mathcal{S}_1, \mathcal{S}_2)$

**Input:**  $\mathcal{S}_1, \mathcal{S}_2, [T]_O^1$  and  $[T]_O^2$

**Output:**  $\mathcal{I}(\mathcal{S}_1, \mathcal{S}_2)$

- 1: Using inputs, obtain a box  $\mathcal{B}_1$  ( $\mathcal{B}_1 \in \mathbb{R}^3$ ) enveloping  $\mathcal{S}_1 \cup \mathcal{S}_2$  in  $\mathbb{R}^3$ ;
- 2: Populate  $\mathcal{H}_1$ , ( $\mathcal{H}_1 \in \mathcal{B}_1$ ), an array of  $N_n$  **uniformly distributed** random triplets in  $\mathbb{R}^3$  (given by  $f_U(x_i)$ ,  $i = 1, 2, 3$ );
- 3: Use naive MC search to check if  $\mathcal{H}_1(j, :) \in \mathcal{S}_1 \cap \mathcal{S}_2$  by using equation (23);
- 4: Save successful trials,  $\mathcal{M}_n(i, :) \leftarrow \mathcal{H}_1(j, :)$  ;
- 5: Obtain box  $\mathcal{B}_2$  from the ranges of columns of  $\mathcal{M}_n$  ;
- 6:  $\mu \leftarrow$  center of  $\mathcal{B}_2$
- 7:  $X_b \leftarrow \mathcal{B}_2^x$ ,  $Y_b \leftarrow \mathcal{B}_2^y$ ,  $Z_b \leftarrow \mathcal{B}_2^z$  ;
- 8:  $\vec{s} = 0.25[X_b, Y_b, Z_b]$ ;
- 9:  $\Sigma \leftarrow S_3$
- 10: Populate  $\mathcal{H}_2$ , an array of  $N_v$  **normally distributed** random triplets in  $\mathbb{R}^3$  using  $\mu$  and  $\Sigma$  from a multi-variate normal PDF (given by  $f_N(x_i)$ ,  $i = 1, 2, 3$ );
- 11: Use importance sampling MC to check  $\mathcal{H}_2(j, :) \in \mathcal{S}_1 \cap \mathcal{S}_2$  also,  $\mathcal{F}(\mathcal{H}_2(j, :)) \rightarrow 1$ ;
- 12: Save successful trials,  $\mathcal{M}_{vr}(i, :) \leftarrow \mathcal{H}_2(j, :)$  for representation;
- 13: Obtain an estimate  $\mathcal{I}(\mathcal{S}_1, \mathcal{S}_2)$  of the intersection volume as  $\langle \mathcal{I} \rangle = \frac{1}{N_v} \sum_{i=1}^{N_v} \mathcal{F}(\mathcal{H}_2(i, :)) \frac{f_U(\mathcal{H}_2(i, :))}{f_N(\mathcal{H}_2(i, :))}$ ;

**Algorithm 2:** Pseudo-code for evaluating intersection volume of two arbitrarily oriented super-ellipsoids in  $SE(3)$

In algorithm 2,  $\mathbf{B}(i, :)$  and  $\mathbf{B}(:, i)$  mean the  $i^{th}$  row and column of the matrix  $\mathbf{B}$  respectively,  $\mathbf{S}_3$  is the  $3 \times 3$  diagonal matrix with the diagonal elements from the vector  $\vec{s}$  in order, and  $\mathcal{B}^x$  is the range of the box  $\mathcal{B}$  in  $X$  Cartesian direction. The above algorithm was used on super-ellipsoid models of index finger and the thumb as given in table 3. To obtain the intersection volume numerically using the algorithm given above, we need to set a cut-off volume above which the thumb and index finger is considered to be collision. This is assumed to correspond to a penetration depth of 0.9 mm – references [48] and [49] report that for human finger, a normal force of 0.5N is obtained at the finger tips for a penetration depth of approximately 0.9mm. It is assumed that this force does not hinder the assembly of the manipulator at the certain given configuration and therefore the solution of the inverse kinematics problem exists at the said configuration. Considering this, the approximate *cutoff* volume is set as  $15 \text{ mm}^3$ . Figures 6a and 6c shows the intersection of two super-ellipsoids in space. The blue box in figures 6b and 6d contains the intersection volume and is aligned along the principal components of the cloud of points  $\mathcal{M}_n$  as obtained in algorithm 2. The intersection volume is detected as  $1041.5 \text{ mm}^3$  for the first case (in figure 6a), thus the chosen orientation of the super-ellipsoids is impossible. However, for the second case (figure 6c) the intersection volume is obtained as  $12.4 \text{ mm}^3$ , thus indicating the chosen orientation of the super-ellipsoids is possible.

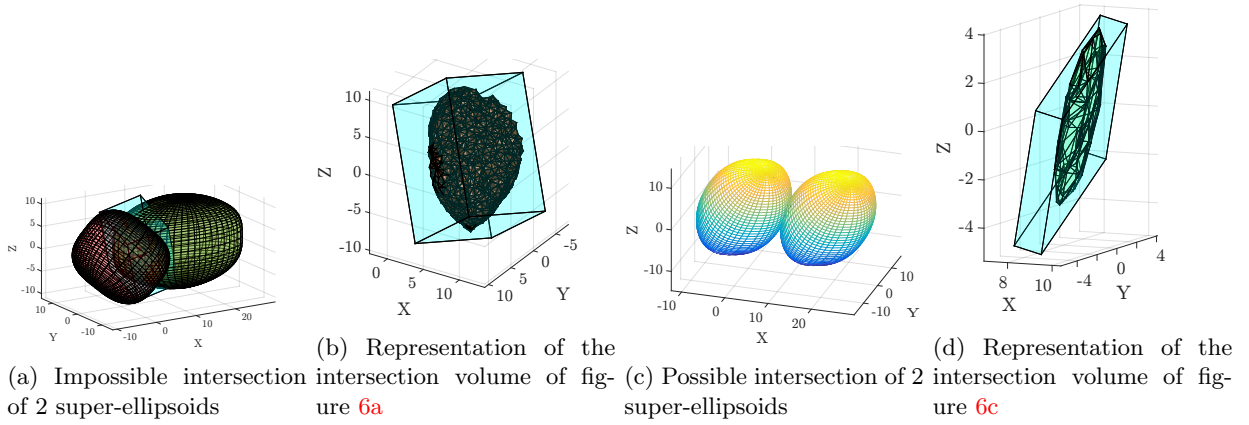


Figure 6: Representation of 2 cases of interaction between super ellipsoids and their intersection volumes

### 3.5 Dexterous manipulation of objects using rolling contacts

To obtain the workspace when rolling without slipping is permitted at the contact between the fingers and the grasped object, we propose an approach based on the existence of the solution of the inverse kinematics problem of the human hand posed as a hybrid parallel manipulator, condition number of the equivalent Jacobian, experimental information about common three fingered dexterous manipulation tasks (see section 4.1) and equations of rolling (see appendix A). Figure 7a describes the finger and the object both modeled as super-ellipsoids in contact at the point  $C$ . Axes with suffixes  $f$  and  $o$  are contiguous to the finger and the object, respectively,  $O_G$  is the origin of global coordinate frame in  $\mathbb{R}^3$  and  ${}^G\mathbf{P}_C$  is the vector joining the point of contact  $C$  with  $O_G$ .  $\mathcal{S}_f$  and  $\mathcal{S}_o$  are the functions that map the 2 dimensional parameter-space  $\{u_i, v_i\}$  to *smooth* and *closed* super-ellipsoids in  $\mathbb{R}^3$  using equations (20) to (22). We define quantity  $\psi$ , as the heading angle, which gives the angle by which the finger frame has to be rotated about the common normal ( $\overline{Z_f Z_o}$  in figure 7a) to align  $X_o$  and  $X_f$ . Due to the contact at  $C$ , no motion is possible along the common normal  $\overline{Z_f Z_o}$ , therefore, the five other possible motions are solved with respect to the 4 parameters describing the contact point on  $\mathcal{S}_f$  and  $\mathcal{S}_o$  and the heading angle. A brief formulation of the problem of obtaining the evolution of the contact points and heading angle i.e.,  $\{u_f, v_f, u_o, v_o, \psi\}^T$  as the object rolls on the fingertips is given in appendix A.

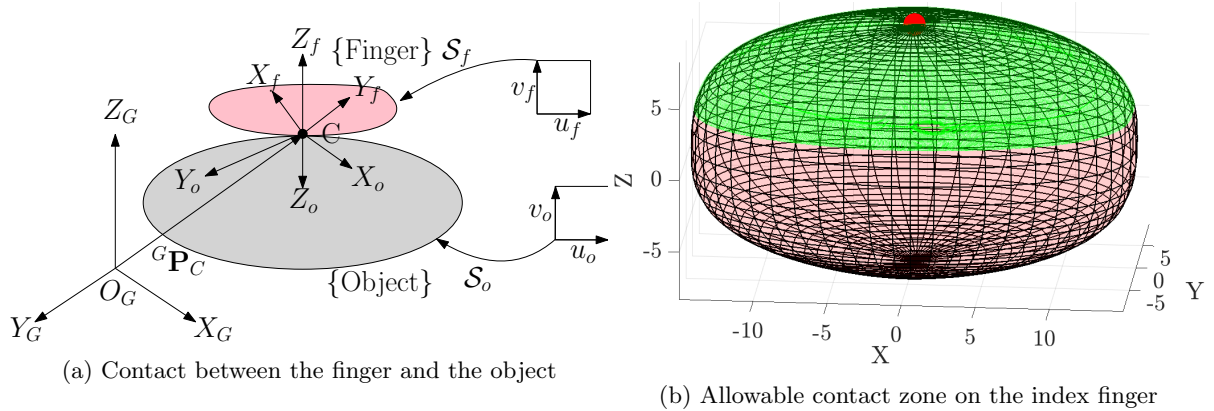


Figure 7: Description of two bodies in contact and permissible contact zone on fingertip

To obtain the evolution of  $\{u_f, v_f, u_o, v_o, \psi\}^T$ , using equations (38) to (40) given in appendix A, we need

the initial conditions for  $\{u_f, v_f, u_o, v_o, \psi\}^T$  and the velocities of the fingertip with respect to the object in contact, i.e.,  $\{\omega_x, \omega_y, \omega_z\}$  and  $\{v_x, v_y\}$ . Using terms for Jacobian from equations (17) and (18) we can solve for all the joint rates (both actuated and passive) for a finger from the equation

$$\begin{Bmatrix} V_{obj} \\ \Omega_{obj} \end{Bmatrix} = \begin{bmatrix} \mathbf{J}_v \\ \mathbf{J}_\omega \end{bmatrix} \begin{Bmatrix} \dot{\vec{\theta}} \\ \dot{\vec{\phi}} \end{Bmatrix} \quad (28)$$

where  $\{\dot{\vec{\theta}}, \dot{\vec{\phi}}\}$  denote the active and passive joints, respectively. It maybe noted that the system in equation (28) is not square, therefore, we opt for least squares solution [50].

Using the values of  $\{V_{obj}, \Omega_{obj}\}^T$  from section 4.1 in equation (28), we can obtain the angular and linear velocities of each fingertip, and therefore the expressions for  $\{\omega_x, \omega_y, \omega_z\}$  and  $\{v_x, v_y\}$  for each of the three fingers with respect to the object. The initial value for  $\psi$  may be obtained as the angle  $\xi_Z$  measured about  $Z_S$  in figure 2a. The initial values for  $\{u_f, v_f, u_o, v_o\}$  are chosen so that the motion starts when the contact is at the center of the finger which is shown as a red disk in figure 7b. The green zone indicates the zone in which the contact is allowed between the object and the finger.

### 3.6 Algorithm to obtain the well-conditioned workspace for the human hand

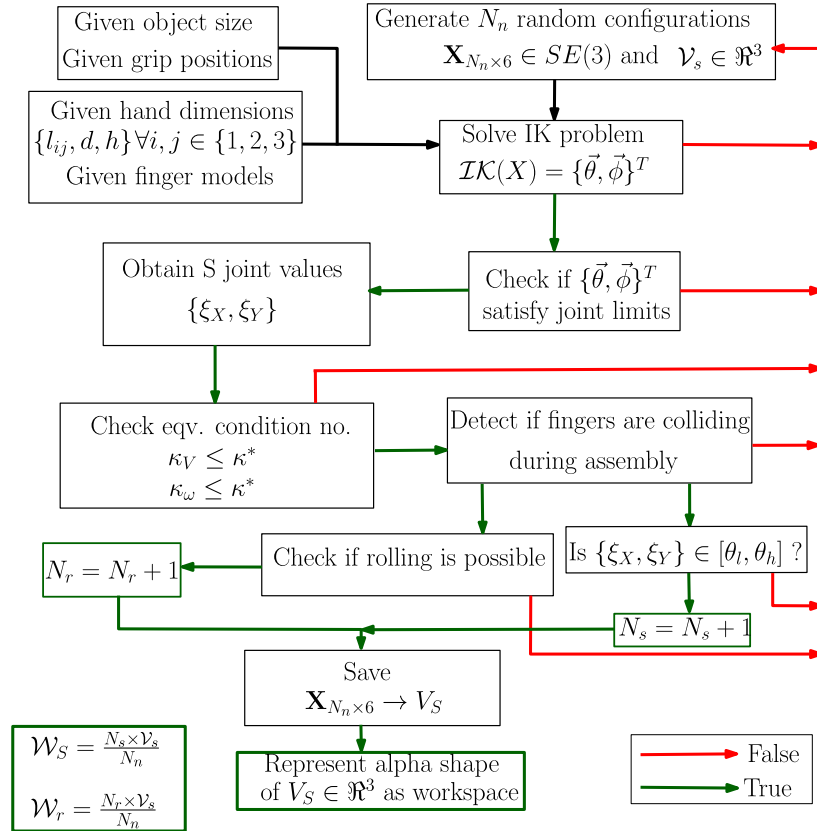


Figure 8: Flowchart of the proposed algorithm to obtain workspace.  $[\theta_l, \theta_h]$  is the permissible range for the spherical joints.

Figure 8 shows the algorithm we have used to obtain the volume and representation of the workspace

of the under two types of contacts. For a given object size, and grip positions (see figure 4b) and given hand dimensions (see, for example, table 1) and finger tip models (see table 3), we define a search space  $\mathcal{V}_s$  in  $\mathbb{R}^3$ . Then we generate  $N_n$  random configurations  $\mathbf{X} \in SE(3)$  where, the Cartesian variables are uniformly distributed in  $\mathcal{V}_s$  and the Euler angles are uniformly distributed in  $[-\pi/2, \pi/2]$ . At each of these configurations, the algorithm in figure 8 is executed. Each of the blocks of the algorithm have either true or false as output, depending on the success and failure of the check undertaken by the block. Success in the check prompts a movement to the next block, in case of a failure, the configuration is rejected and a new configuration is generated and the check starts afresh. If a configuration passes through all the checks a counter value ( $N_s$  or  $N_r$  depending upon the type of workspace required) is increased and the configuration is saved for representation. However the arrangement of the different checks suggested in figure 8 is not unique and the particular arrangement has been chosen for better computational performance<sup>7</sup>.

The blocks, as shown in figure 8, are coded to perform different checks independent of each other, with the inputs being hand dimensions and joint angles obtained from supplied data and solution of the IK problem. Therefore, the IK problem has to be solved for all  $N_n$  points for the three fingers and each evaluation of the IK problem for the fingers takes a time of the order of  $3 \times 10^{-4}$  seconds which is quite fast because of the symbolic implementation used. Next, we check if the chosen configuration is well conditioned or not by evaluating the condition number of the equivalent Jacobians (see equation (19)) and ensuring that they are less than 1000 at all times. This takes about  $28.63 \times 10^{-3}$  seconds due to the symbolic implementation of the total process. Simultaneously, we also obtain the S joint values, which takes  $1.58 \times 10^{-4}$  seconds. Next we check for fingertip collisions, which takes about 0.73 secs. Finally, we check for the possibility of rolling the given object on the fingertips, which takes about 1.95 secs per iteration. A fully parallel implementation of the algorithm to obtain the workspaces of a parallel manipulator by checking through 150,000 random configurations of the end effector takes about 624 seconds.

## 4 Numerical experiments and results

In this section we will discuss a few numerical experiments using the methodology developed so far, to get some insight into the design of the human hand and kinematics of dexterous manipulation using a parallel manipulator framework as described in section 3.1. We will start by discussing some physical insights obtained through experiments on dexterous manipulation and use those to design our numerical experiments. Following which we will discuss the numerical experiments and results obtained from the same.

### 4.1 Experimental insights into dexterous manipulation

In this section we discuss some experiments on human dexterous manipulation, to gain some insights on the range of motion and the speeds attainable during an in-hand manipulation task attainable by an individual. For recording the motion of the object we have used a [52] electromagnetic position tracker, which can log the position and orientation of an object in real time. The configuration of the object are obtained by rigidly fixing a *sensor* to it and logging the values of the 6 channels per sensor, 3 for absolute position and 3 for absolute orientation of the sensor with respect to the source of the magnetic field. We briefly describe our experimental procedure below.

**Experiment:** At first the wrist of a healthy adult subject is immobilized by splints and bandages to restrict all the 4 motions of the wrist viz. radial and ulnar deviations, palmar extension and flexion. Next, a tracking sensor is fixed approximately at the base of the trapezium bone (point  $B_0^3$  in figures 1b and 3) on the dorsal side of the hand, and another tracking sensor is fixed approximately at the center of a spherical object to be used for the manipulation task. Figure 9a shows the location of the tracking sensors on the hand and the object during a manipulation task. We have used a standard ping-pong ball ( $\sim 40$ mm dia.) and a standard tennis ball ( $\sim 65$ mm dia.) for our manipulation tasks. The subject is asked to manipulate

<sup>7</sup>Computational performances are measured as CPU times are for Matlab<sup>®</sup> 2015a[51] run in a 64bit Windows 7 PC with a Intel XEON processor (4 cores @ 3.10 GHz) and 16GB RAM

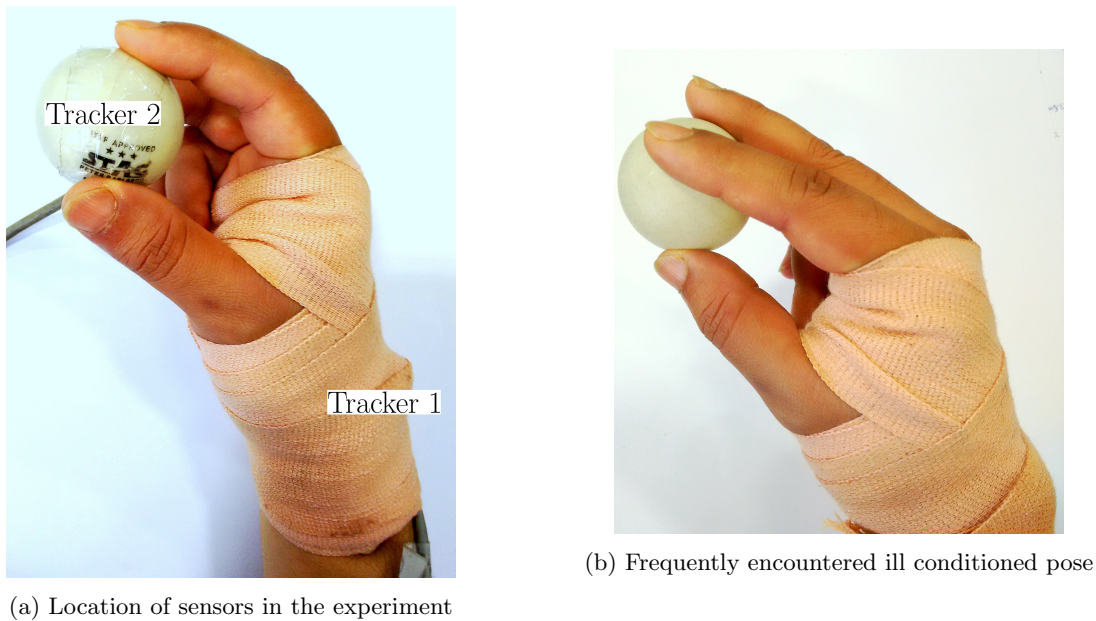


Figure 9: Location of sensors on the hand and a known ill conditioned pose

the object at *normal* speed while taking notice all three fingers are contacting the object at all times and the point of contacts are within the permissible zone as indicated in figure 7b. The manipulation task is usually about 60 to 100 seconds long and configuration data is logged for both the sensors at 120 Hz throughout the duration of the experiment.

**Data collection and post-processing:** The data collected from the sensors are quite noisy with typical values of signal-to-noise ratios of 1.5 to 2 dB. The poor quality of the signals is chiefly attributed to interfering magnetic fields from various sources nearby to the channel. The channel noises for a sensor are found to be normally distributed with zero mean and standard deviations ranging between 0.003 to 0.03. To de-noise the channel signals we have used the method of non-local means (see e.g. [53] and the `Matlab` implementation of the same by [54]). The de-noised signal is then used to obtain configuration of the manipulated object with respect to the frame attached to the hand. Subsequently the gradients of the relative position and orientation of the object are represented as the linear and angular velocities of the manipulated object.

**Results:** From the analysis of the data from experiments with 5 male subjects we have obtained the following results:

- The manipulation area was bounded by the positive Cartesian octant, with slight deviations of the order of 2-3 mm along the  $Y$  direction.
- The orientations possible for the object was at most  $\pm 90^\circ$  about an axis, with actual in-task motions ranging between  $\pm 10^\circ$  (see figure 11b).
- Figure 10 shows the velocities attained by the ball in 3 separate experiments. The black lines show the velocities obtained by a subject ( $M_{30}$ ) manipulating a table tennis ball, the orange line shows the velocities obtained by a different subject ( $M_{24}$ ) manipulating the same ball and the green line shown the second subject manipulating a tennis ball. From the experiment we can conclude that there is *not much* variation in the velocities achieved by different subjects across two different manipulation tasks.
- Therefore, from figure 10 we obtain  $V_x = V_y = V_z = 0.1\text{m/s}$  and  $\omega_x = \omega_y = \omega_z = 0.1\text{rad/s}$ , which are used in equation (28) to obtain the joint rates of the manipulator for achieving the target velocities at the end effector.

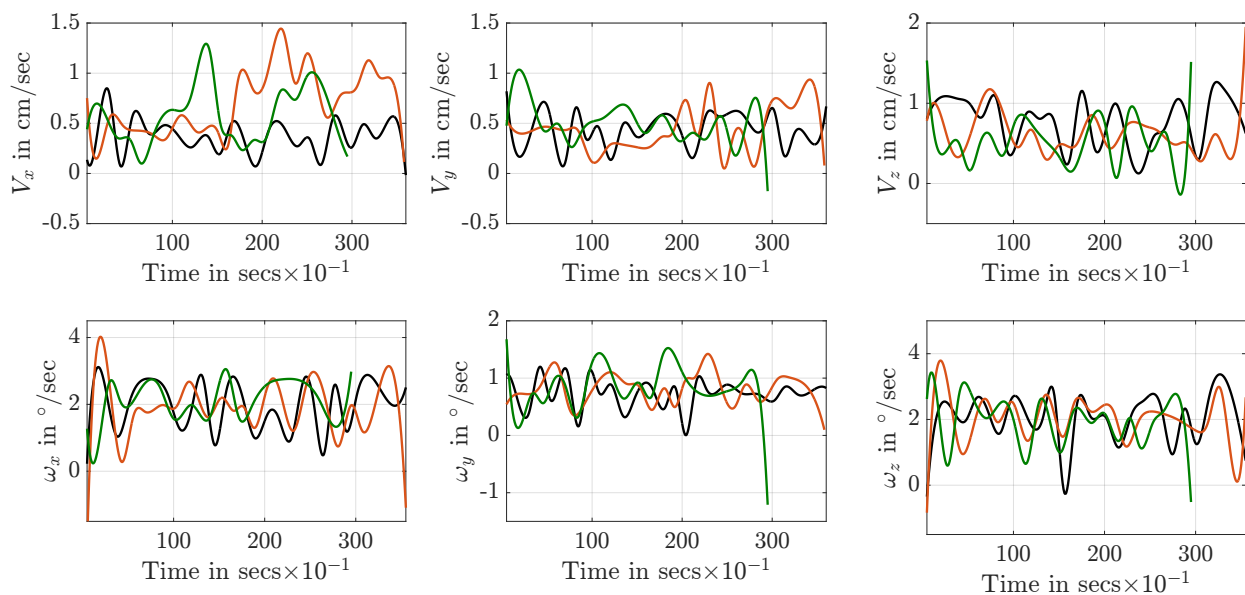
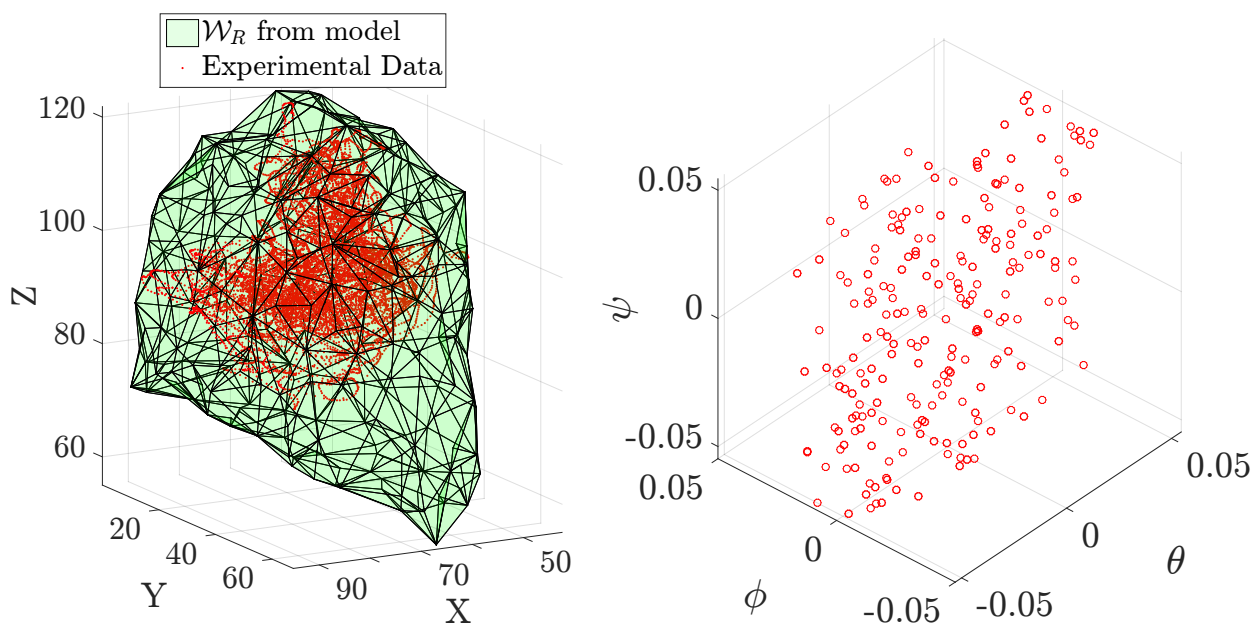


Figure 10: Typical velocities encountered during 3 different dexterous manipulation tasks shown in 3 colors

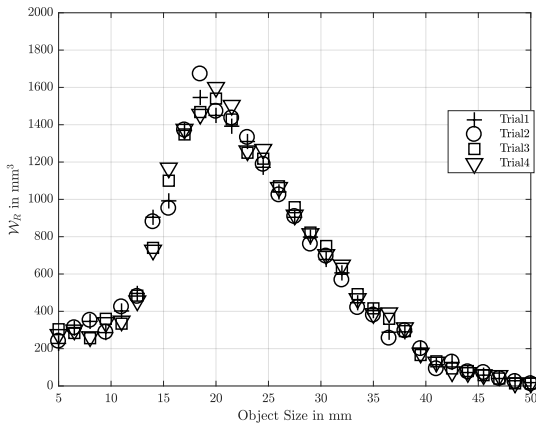


(a) Comparison of the theoretically and experimentally obtained workspaces

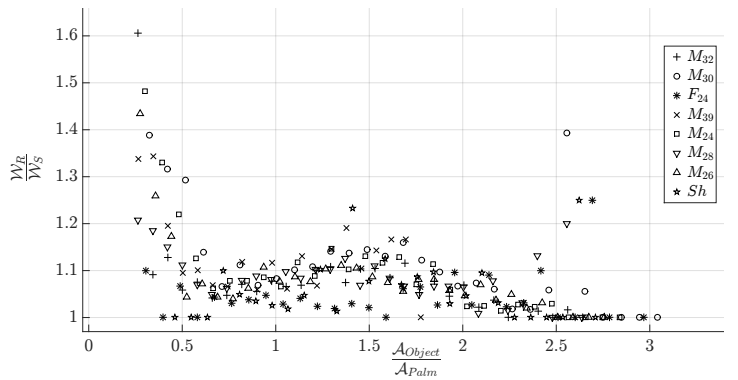
(b) Orientations achieved in experiments

Figure 11: Experimental results on human hand workspaces

Figure 11 shows the position and orientation data obtained from experiments. The position workspace (figure 11a) obtained from the experiments, when compensated for the sensor dimensions and wrist thickness *almost* entirely fits into the theoretically obtained workspace, barring a few points obtained due to un-modeled motion of the fingers like possible motion of the joint  $B_3^1$  beyond  $90^\circ$ , possible slipping



(a) Convergence of the algorithm across 4 different trials



(b) Variation of  $\frac{W_R}{W_S}$  with change in object size

Figure 12: Convergence of the algorithm and variation of  $\frac{W_R}{W_S}$  with change in object size

and temporary detachment of the index finger during the motion and some ill conditioned poses attained frequently during the manipulation task (see e.g. figure 9b where  $\kappa_V \rightarrow \infty$ ). The inclusion of the experimentally obtained workspace in the theoretically obtained workspace, and the fact that the theoretically obtained workspace puts a reasonably conservative bound on the experimental workspace (see figure 11a) may demonstrate the correctness of our modeling approach. However, it may also be noted that the experimentally obtained may never supersede the theoretically obtained one by large amounts because though we are using practically possible joint limits (see table 2), actual motions possible during a dexterous manipulation task are somewhat less than obtained maximal joint limits of each individual finger. We also do not consider the motion of the wrist and the orientations obtained by moving the wrist in the simulations.

## 4.2 Modeling the human hand kinematics and obtaining the workspaces

In this section we discuss the results we have obtained with our modeling. Through our algorithm as described in figure 8 we seek  $W_R$ , the available *well conditioned* workspace considering rolling type of contact at the fingertips and  $W_S$ , the available *well conditioned* workspace considering S joint type of contact between the object and the fingertips. In each case, we start by defining the initial contact points as the vertexes of an equilateral triangle inscribed by the object modeled as a sphere. The search space  $\mathcal{V} \in \mathbb{R}^3$  is a box bounded by the planes  $X = (0, 100)$ ,  $Y = (0, 100)$  and  $Z = (50, 150)$  (in mm), and the orientation search space in  $SO(3)$  is bounded by  $\{\theta, \phi, \psi\} \in [-90^\circ, 90^\circ]$ . Figure 4b shows the snapshot of the simulation for obtaining  $W_R$  for a particular configuration of the object.

In figure 12a we show that our algorithm converges across 4 different trials for a particular set of hand dimensions. We have evaluated the algorithm for 60 object sizes ranging from 1mm diameter to 40mm diameter. We also observe from figure 12b that the ratio  $r_{RS} = \frac{W_R}{W_S}$  also converges across different subjects and trials. Figure 13 shows the possible positional and orientation workspaces of the manipulator. We note from figure 13a that  $W_S$  is smaller than  $W_R$  and is inscribed in the same and the maximum orientation workspace shown in figure 13b is not very significant for a dexterous manipulation task with a spherical object due to its symmetry. We have included figure 13b to demonstrate that the entire workspace  $\mathcal{W}$ ,  $\mathcal{W} \in SE(3)$ , can be obtained and represented by our algorithm.

From observations in daily life, the experiments in section 4.1 and results obtained so far we observe that the values of  $W_R$  and  $W_S$  vary widely with change in object size. Therefore, using the developments

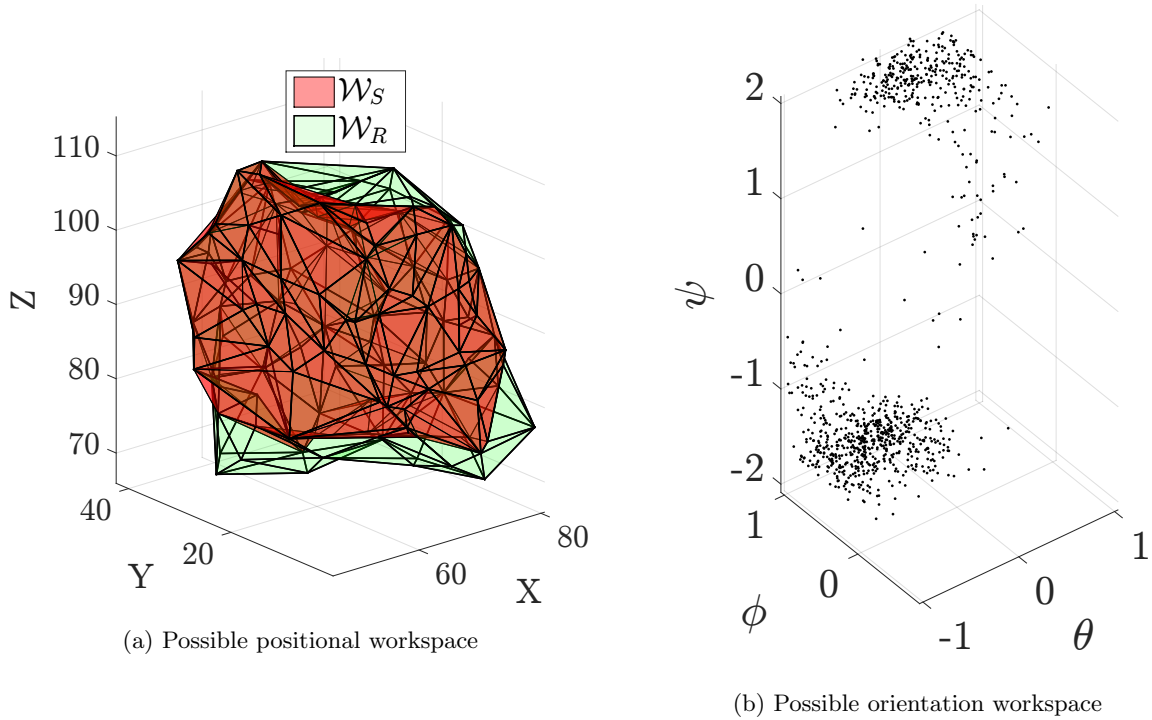
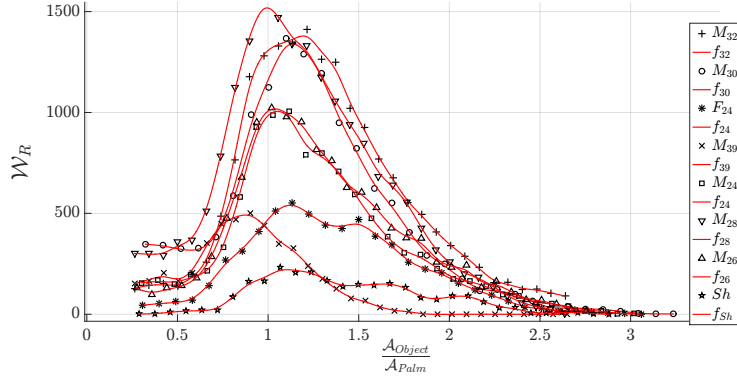


Figure 13: Workspaces of hand described in tables 1 to 3 manipulating a ball of radius 17.5 mm

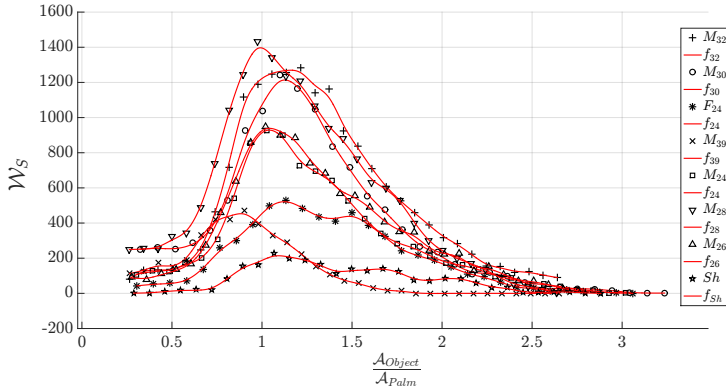
so far, we try to obtain a relationship between the *best* cross sectional area of a spherical object ( $\mathcal{A}_{object}$ ) for dexterous manipulation and the human hand dimensions. For this we chose the palm area, area of the  $\triangle B_1^0 B_2^0 B_3^0$  in figure 3 denoted by  $\mathcal{A}_{palm} = d \times h$ , as a characteristic dimension of the human hand and obtain the values of  $\mathcal{W}_R$  and  $\mathcal{W}_S$  with varying palm area-object area ratios  $r_{po} = \frac{\mathcal{A}_{palm}}{\mathcal{A}_{object}}$ . We choose 8 data sets designated as  $\{M_{32}, M_{24}, M_{26}, M_{28}, M_{30}, M_{39}, F_{24}, Sh\}$  denoting the hand dimensions of 6 adult male subjects, 1 female subject and the Shadow hand (see [9]) respectively  $f$  with suffixes in the figure represent the quartic polynomials fitted to the obtained data sets as given in figures 14a and 14b. The models for the fingertips for the male subjects were scaled up/down from the model developed in section 3.4.1 and a separate model was obtained for the female subject's hand by the technique discussed in section 3.4.1. The finger models and hand dimensions for the Shadow hand were obtained from specifications laid down by the [9]. For each of the subjects values of  $\mathcal{W}_R$  and  $\mathcal{W}_S$  were obtained for 60 object sizes across 4 separate trials, their convergence was ensured and the combined data is plotted in figure 14. A summary of the results is given in table 4. From the table we can conclude that the human hand can attain the highest workspace for a spherical object when the object cross section area is *approximately* equal to the palm area. Figure 14c shows that the results in table 4 is independent of the bounds on the condition number imposed by us in equation (19).

Table 4: Means and standard deviations of  $r_{po}$  for the maximum workspace

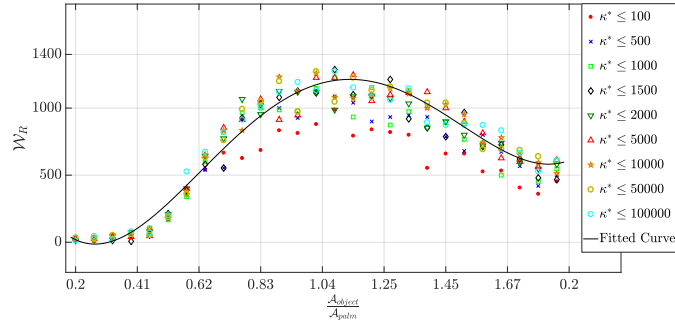
Type of contact	$r_{po}^-$	$\sigma(r_{po})$
Rolling type	$r_{po}^- = 1.004$	$\sigma(r_{po}) = 0.0443$
S joint type	$r_{po}^- = 1.016$	$\sigma(r_{po}) = 0.0761$



(a) Rolling Workspace



(b) S-joint workspace



(c) Independence of the result in table 4 to choice of condition number in equation (19)

Figure 14: Comparison of workspaces of hand considering two different models of contact across different hands

### 4.3 Effect of human hand dimensions on the hand workspace

From figure 14 we observe that the available workspaces for hands of different sizes vary widely and for manipulating the same object a *larger* hand has a larger workspace. Therefore, to analyze the dependence of the human hand workspace volume on individual hand dimensions like finger lengths and palm area etc. we pose the following problem:

**Problem** To obtain the dimensions of the 95<sup>th</sup> percentile male human hand with the largest well condi-

tioned workspace area while manipulating a spherical object of a given size.

**Solution** To solve the problem, we parametrize the hand (as shown in figure 3) with the dimensions as shown in equation (29).

$$\mathbf{P} = \{d, h, l_{11}, l_{12}, l_{13}, r_m = \sum_{i=1}^3 l_{2i} / \sum_{i=1}^3 l_{1i}, r_t = \sum_{i=1}^3 l_{3i} / \sum_{i=1}^3 l_{1i}\} \quad (29)$$

Next, we formulate the following optimization problem as shown in equation (30).

$$\begin{aligned} & \underset{\mathbf{P}}{\text{Maximize}} \mathcal{W}_S(\mathbf{P}) \\ & \text{Subject to} \quad h \times d \leq 1000, \quad \sum_{i=1}^3 l_{1i} = 80 \\ & \quad r_m < 2, \quad r_t < 2, \quad l_{1i} \geq 20, \quad \forall i = 1, 2, 3 \\ & \quad d > 0, \quad h > 0, \quad d \leq 20, \quad h \leq 80 \ \& \ d \leq 0.3h \end{aligned} \quad (30)$$

The constraints as well as their numerical values have been obtained for the 95<sup>th</sup> percentile male according to the studies by [55] and [56]. The constrained optimization problem is solved and the optimum value of  $\mathbf{P} = \vec{\mathcal{P}}$  is obtained. The Lagrange multipliers for the equality and inequality constraints are also obtained at the optimum. A scaled plot containing the constraint Lagrange multipliers is given in figure 15. At an optimum point  $\vec{\mathcal{P}}$ , the Lagrange multipliers give the effect of the perturbation on the constraints. Any positive perturbations to the constraints associated with the negative Lagrange multipliers will increase the value of the objective function from the value obtained at an optimum [57]. Therefore, from figures 3 and 15, we can conclude the following:

- The constraints limiting the hand size i.e., palm area and index finger length given by  $l \times d < 1000$  and  $\sum_{i=1}^3 l_{1i} = 80$ , have negative Lagrange multipliers associated with them, which signifies the obvious result that a *larger hand* has a larger workspace.
- From the value of the Lagrange multipliers for the constraints we observe that the workspace is more sensitive to a change in palm area than a change in finger length.
- The workspace is not very sensitive to the upper limits on  $r_m$  and  $r_t$ . Also, at an optimum we obtain  $r_m = 1.1$  and  $r_t = 1.35$  which are quite close to the values suggested by [56] and [55].
- The workspace is quite sensitive to lower bounds on the fingers segments, however, the workspace is not sensitive to the lower limits on  $d$  and  $h$ .
- Values of the Lagrange multipliers associated with constraints on the upper limits on  $d$  and  $h$  suggest that the workspace is equally sensitive to these constraints.

## 5 Conclusion

In this work, the focus has been on understanding dexterous manipulation of a multi-fingered human hand grasping an object. In section 1, a comprehensive review of the current state-of-the-art in the topic is presented and in section 2, we have presented an overview of a Monte Carlo based probabilistic technique used to obtain the workspace of object grasped by a multi-fingered hand. The human hand grasping an object has been modeled in two ways, namely point contact with friction and a contact allowing rolling without slipping. In both these situations, we model the three-fingered hand grasping a sphere as a hybrid parallel manipulator with six degrees of freedom and present an algorithm to obtain the well conditioned

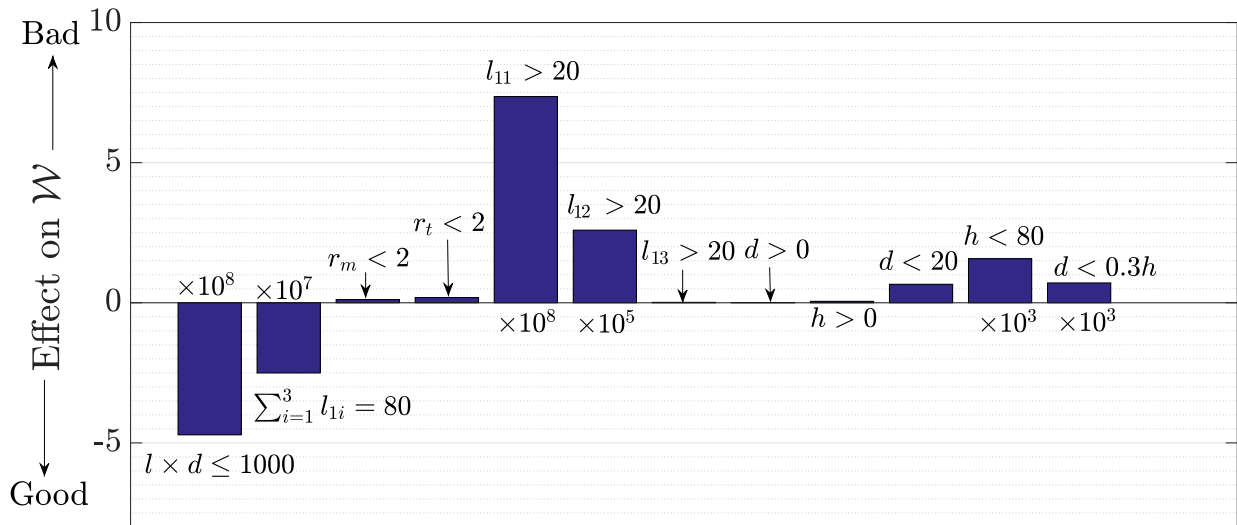


Figure 15: Scaled plot showing effects of constraints on hand workspace

workspaces of the hybrid parallel manipulators. The main results are presented in section 4 and we show that the maximum workspace of the grasped object is obtained when the palm size is same as the grasped object size. We also show that the maximum workspace could be as much 1.5 times when rolling without slipping is allowed. In section 4.1, experimental results on dexterous manipulation are presented to set a perspective for the numerical experiments and to make them more realistic are described. It is shown that the experimental results agree reasonably well with numerical simulation results. The numerical results also show the sensitivity of the obtained workspace due to changes in its geometry. In this paper, we have attempted to comprehensively address the issues in kinematics of dexterous manipulation. However, several aspects such as dynamics, control and path planning problems related to dexterous manipulation remain unexplored and are future avenues of research.

## Acknowledgement

We wish to thank Prof. Dibakar Sen of the Department of Mechanical Engineering, IISc Bangalore, for allowing us to use the Polhemus-Liberty electromagnetic tracker. The experiments in section 4.1 were done using this device in his laboratory.

## A Appendix I: Equations of rolling after Montana[15]

The common normal  $\mathbf{n}$ , to the surfaces  $\mathcal{S}_f$  and  $\mathcal{S}_o$  (in figure 7a) is given in equation (31) according to [42].

$$\begin{Bmatrix} n_x \\ n_y \\ n_z \end{Bmatrix} = \begin{Bmatrix} \frac{\operatorname{sgn}(\cos(v)) (|\cos(v)|)^{2-n} \operatorname{sgn}(\cos(u)) (|\cos(u)|)^{2-e}}{\operatorname{sgn}(\cos(v)) (|\cos(v)|)^{2-n} \operatorname{sgn}(\sin(u)) (|\sin(u)|)^{2-e}} \\ \frac{B}{\operatorname{sgn}(\sin(v)) (|\sin(v)|)^{2-n}} \\ C \end{Bmatrix} \quad (31)$$

Using equations (20) to (22) we can obtain a parametric expression for the surface as  $\mathbf{f}(u, v) = \begin{Bmatrix} x(u, v) \\ y(u, v) \\ z(u, v) \end{Bmatrix}$ .

At a point  $P_0$  on the surface we define a orthogonal frame  $\mathbf{H}$  as

$$\mathbf{H} = \begin{Bmatrix} \frac{\mathbf{f}_u}{|\mathbf{f}_u|} \\ \mathbf{f}_{v^*} \\ \mathbf{n} \end{Bmatrix} \quad (32)$$

In equation (32),  $\mathbf{f}_{v^*} = \frac{\mathbf{n}}{|\mathbf{n}|} \times \frac{\mathbf{f}_u}{|\mathbf{f}_u|}$ <sup>8</sup> and  $\mathbf{k}(\cdot) = \frac{\partial \mathbf{k}}{\partial(\cdot)}$  and the value of the contact normal  $\mathbf{n}$  is obtained from equation (31). Based on  $\mathbf{H}$  in equation (32) we can define the following metric  $[\mathbf{M}]$ , curvature form  $[\mathbf{K}]$  and torsion form  $[\mathbf{T}]$  for each of the surfaces  $\mathcal{S}_f$  and  $\mathcal{S}_o$  as:

$$[\mathbf{M}] = \begin{bmatrix} |\mathbf{f}_u| & 0 \\ 0 & |\mathbf{f}_{v^*}| \end{bmatrix} \quad (33)$$

$$[\mathbf{K}] = \begin{bmatrix} \frac{\mathbf{f}_u \cdot \mathbf{n}_u}{|\mathbf{f}_u|^2} & \frac{\mathbf{f}_u \cdot \mathbf{n}_{v^*}}{|\mathbf{f}_u| |\mathbf{f}_{v^*}|} \\ \frac{\mathbf{f}_{v^*} \cdot \mathbf{n}_u}{|\mathbf{f}_u| |\mathbf{f}_{v^*}|} & \frac{\mathbf{f}_{v^*} \cdot \mathbf{n}_{v^*}}{|\mathbf{f}_{v^*}|^2} \end{bmatrix} \quad (34)$$

$$[\mathbf{T}] = \begin{bmatrix} \frac{\mathbf{f}_{v^*} \cdot \mathbf{f}_{uu}}{|\mathbf{f}_u|^2 |\mathbf{f}_{v^*}|} & \frac{\mathbf{f}_{v^*} \cdot \mathbf{f}_{uv^*}}{|\mathbf{f}_{v^*}|^2 |\mathbf{f}_u|} \end{bmatrix} \quad (35)$$

In equation (35),  $\mathbf{f}_{uv^*} = \mathbf{f}_{v^*u} = \frac{\partial}{\partial u} \left( \frac{\mathbf{n}}{|\mathbf{n}|} \times \frac{\mathbf{f}_u}{|\mathbf{f}_u|} \right)$ .

Also in equation (34),  $n_{v^*} = \mathbf{n}_u u_{v^*} + \mathbf{n}_v v_{v^*}$ , where, a *least squares estimate* values of  $u_{v^*}$  and  $v_{v^*}$  can be obtained by comparing the components of both left and right sides of equation (36).

$$\mathbf{f}_{v^*} = \frac{\mathbf{n}}{|\mathbf{n}|} \times \frac{\mathbf{f}_u}{|\mathbf{f}_u|} = \mathbf{f}_u \frac{\partial u}{\partial v^*} + \mathbf{f}_v \frac{\partial v}{\partial v^*} \quad (36)$$

Again,

$$[R_\psi] = \begin{pmatrix} \cos \psi & -\sin \psi \\ -\sin \psi & -\cos \psi \end{pmatrix}, \quad [\mathbf{K}_f^*] = [R_\psi][\mathbf{K}_f][R_\psi]^T \quad (37)$$

Using equations (33) to (35) and (37) we can write the equations of motion of two bodies in contact undergoing *rolling* after [15] as,

$$(\dot{u}_o, \dot{v}_o) = [\mathbf{M}_o]^{-1}([\mathbf{K}_o] + [\mathbf{K}_f^*])^{-1}[\{-\omega_y, \omega_x\}^T - [\mathbf{K}_f^*]\{v_x, v_y\}^T] \quad (38)$$

$$(\dot{u}_f, \dot{v}_f) = [\mathbf{M}_f]^{-1}[R_\psi]([\mathbf{K}_o] + [\mathbf{K}_f^*])^{-1}[\{-\omega_y, \omega_x\}^T + [\mathbf{K}_o]\{v_x, v_y\}^T] \quad (39)$$

$$\dot{\psi} = \omega_z + [\mathbf{T}_o][\mathbf{M}_o](\dot{u}_o, \dot{v}_o)^T + [\mathbf{T}_f][\mathbf{M}_f](\dot{u}_f, \dot{v}_f)^T \quad (40)$$

Equations (38) to (40) along with  $v_z = 0$  can be solved simultaneously to obtain the evolution of the contact points on the object and the finger.

<sup>8</sup>This re-parametrization is required for the general super ellipse as the vectors  $\{\mathbf{f}_u/|\mathbf{f}_u|, \mathbf{f}_v/|\mathbf{f}_v|, \hat{\mathbf{n}}\}^T$  do not constitute an orthogonal frame

## References

- [1] Ritter, H., and Haschke, R., 2014. “Hands, dexterity, and the brain”. In *Humanoid Robotics and Neuroscience: Science, Engineering and Society*. CRC Press, pp. 49–77.
- [2] Balasubramanian, R., and Santos, V. J., 2014. *The Human Hand as an Inspiration for Robot Hand Development*, Vol. 95. Springer.
- [3] Okamura, A. M., Smaby, N., and Cutkosky, M. R., 2000. “An overview of dexterous manipulation”. In *Robotics and Automation, 2000. Proceedings. ICRA’00. IEEE International Conference on*, Vol. 1, IEEE, pp. 255–262.
- [4] Hanafusa, H., and Asada, H., 1977. “A robot hand with elastic fingers and its application to assembly process”. In *Proc. IFAC Symp. Inform. Contr. Prob. Manufact. Tech.*, pp. 127–134.
- [5] Salisbury, J. K., and Craig, J. J., 1982. “Articulated hands: Force control and kinematic issues”. *The International Journal of Robotics Research*, **1**(1), pp. 4–17.
- [6] Jacobsen, S., Iversen, E., Knutti, D., Johnson, R., and Biggers, K., 1986. “Design of the Utah/MIT dextrous hand”. In *Robotics and Automation. Proceedings. 1986 IEEE International Conference on*, Vol. 3, IEEE, pp. 1520–1532.
- [7] Murray, R. M., and Sastry, S. S., 1989. “Control experiments in planar manipulation and grasping”. In *Robotics and Automation, 1989. Proceedings., 1989 IEEE International Conference on*, IEEE, pp. 624–629.
- [8] Butterfaß, J., Grebenstein, M., Liu, H., and Hirzinger, G., 2001. “DLR-Hand II: Next generation of a dextrous robot hand”. In *Proceedings of ICRA. IEEE International Conference on Robotics and Automation, 2001.*, Vol. 1, IEEE, pp. 109–114.
- [9] Shadow Robot Company, 2013. Shadow Hand. <https://www.shadowrobot.com/products/dexterous-hand/>. Accessed: 2017-03-15.
- [10] Deimel, R., and Brock, O., 2016. “A novel type of compliant and underactuated robotic hand for dexterous grasping”. *The International Journal of Robotics Research*, **35**(1-3), pp. 161–185.
- [11] Deshpande, A. D., and Matsuoka, Y., 2014. “Development of an anatomically correct testbed (ACT) hand”. In *The Human Hand as an Inspiration for Robot Hand Development*. Springer, pp. 453–475.
- [12] Lin, J., Wu, Y., and Huang, T. S., 2000. “Modeling the constraints of human hand motion”. In *Human Motion, 2000. Proceedings. Workshop on*, IEEE, pp. 121–126.
- [13] Dizioğlu, B., and Lakshminarayana, K., 1984. “Mechanics of form closure”. *Acta Mechanica*, **52**(1), pp. 107–118.
- [14] Nguyen, V.-D., 1987. “Constructing stable grasps in 3D”. In *Robotics and Automation. Proceedings. 1987 IEEE International Conference on*, Vol. 4, IEEE, pp. 234–239.
- [15] Montana, D. J., 1988. “The kinematics of contact and grasp”. *The International Journal of Robotics Research*, **7**(3), pp. 17–32.
- [16] Cai, C. S., and Roth, B., 1986. “On the planar motion of rigid bodies with point contact”. *Mechanism and Machine Theory*, **21**(6), pp. 453–466.
- [17] Kerr, J., and Roth, B., 1986. “Analysis of multifingered hands”. *The International Journal of Robotics Research*, **4**(4), pp. 3–17.

- [18] Borràs, J., and Dollar, A. M., 2015. “Dimensional synthesis of three-fingered robot hands for maximal precision manipulation workspace”. *The International Journal of Robotics Research*, **34**(14), pp. 1731–1746.
- [19] Cobos, S., Ferre, M., Uran, M. S., Ortego, J., and Pena, C., 2008. “Efficient human hand kinematics for manipulation tasks”. In *Intelligent Robots and Systems, 2008. IROS 2008. IEEE/RSJ International Conference on*, IEEE, pp. 2246–2251.
- [20] Glasserman, P., 2013. *Monte Carlo Methods in Financial Engineering*, Vol. 53. Springer Science & Business Media.
- [21] Dunn, W. L., and Shultis, J. K., 2011. *Exploring Monte Carlo Methods*. Elsevier.
- [22] Stamper, R. E., Tsai, L.-W., and Walsh, G. C., 1997. “Optimization of a three dof translational platform for well-conditioned workspace”. In *Robotics and Automation, 1997. Proceedings., 1997 IEEE International Conference on*, Vol. 4, IEEE, pp. 3250–3255.
- [23] Tsai, L.-W., Walsh, G. C., and Stamper, R. E., 1996. “Kinematics of a novel three dof translational platform”. In *Robotics and Automation, 1996. Proceedings., 1996 IEEE International Conference on*, Vol. 4, IEEE, pp. 3446–3451.
- [24] Chaudhury, A. N., and Ghosal, A., 2017. “Optimum design of multi-degree-of-freedom closed-loop mechanisms and parallel manipulators for a prescribed workspace using monte carlo method”. *Mechanism and Machine Theory*, **118**, pp. 115–138.
- [25] Fishman, G., 2013. *Monte Carlo: Concepts, Algorithms, and Applications*. Springer Science & Business Media.
- [26] Selig, J. M., 2004. *Geometric fundamentals of robotics*. Springer Science & Business Media.
- [27] Lee, D.-T., and Schachter, B. J., 1980. “Two algorithms for constructing a delaunay triangulation”. *International Journal of Computer & Information Sciences*, **9**(3), pp. 219–242.
- [28] Edelsbrunner, H., and Mücke, E. P., 1994. “Three-dimensional alpha shapes”. *ACM Transactions on Graphics (TOG)*, **13**(1), pp. 43–72.
- [29] Artec3D. Artec3D scanner. <https://www.artec3d.com/3d-scanner/artec-eva>. Accessed: 2017-03-15.
- [30] Nakamura, M., Miyawaki, C., Matsushita, N., Yagi, R., and Handa, Y., 1998. “Analysis of voluntary finger movements during hand tasks by a motion analyzer”. *Journal of Electromyography and Kinesiology*, **8**(5), pp. 295–303.
- [31] Chaudhury, A. N., and Ghosal, A., 2017. “Determination of workspace volume of parallel manipulators using monte carlo method”. In *Computational Kinematics*. Springer, pp. 323–330.
- [32] Degeorges, R., and Oberlin, C., 2003. “Measurement of three-joint-finger motions: reality or fancy? a three-dimensional anatomical approach”. *Surgical and Radiologic Anatomy*, **25**(2), pp. 105–112.
- [33] Degeorges, R., Laporte, S., Pessis, E., Mitton, D., Goubier, J.-N., and Lavaste, F., 2004. “Rotations of three-joint fingers: a radiological study”. *Surgical and Radiologic Anatomy*, **26**(5), pp. 392–398.
- [34] Autodesk-netfabb, 2013. *version 7.4.0 532(2013)*. Autodesk, Inc., Mill Valley, California, USA.
- [35] Cole, A. B., Hauser, J. E., and Sastry, S. S., 1989. “Kinematics and control of multifingered hands with rolling contact”. *IEEE Transactions on Automatic Control*, **34**(4), pp. 398–404.

- [36] Murray, R. M., Li, Z., and Sastry, S. S., 1994. *A Mathematical Introduction to Robotic Manipulation*. CRC press.
- [37] Ghosal, A., 2006. *Robotics: Fundamental Concepts and Analysis*. Oxford University Press.
- [38] Ghosal, A., and Ravani, B., 2001. “A differential-geometric analysis of singularities of point trajectories of serial and parallel manipulators”. *Transactions of the American Society of Mechanical Engineers Journal of Mechanical Design*, **123**(1), pp. 80–89.
- [39] Bardinet, E., Ayache, N., and Cohen, L., 1994. “Fitting of iso-surfaces using superquadrics and free-form deformations”. In *Biomedical Image Analysis, 1994.*, Proceedings of the IEEE Workshop on, IEEE, pp. 184–193.
- [40] Solina, F., and Bajcsy, R., 1990. “Recovery of parametric models from range images: The case for superquadrics with global deformations”. *IEEE Transactions on Pattern Analysis and Machine Intelligence*, **12**(2), pp. 131–147.
- [41] Menon, M. S., and Ghosal, A., 2015. “Obstacle avoidance for hyper-redundant snake robots and one dimensional flexible bodies using optimization”. In *Proceedings of the 14<sup>th</sup> IFToMM World Congress*, October, 2015 Taipei City, Taiwan, pp. 391–397.
- [42] Barr, A. H., 1992. *Rigid physically based superquadrics*. Academic Press Professional, Inc., ch. III.8, pp. 137–159.
- [43] Taubin, G., 1993. “An improved algorithm for algebraic curve and surface fitting”. In *Computer Vision, 1993. Proceedings.*, Fourth International Conference on, IEEE, pp. 658–665.
- [44] Boyd, S., and Vandenberghe, L., 2004. *Convex Optimization*. Cambridge university press.
- [45] Agarwal, S., Srivatsan, R. A., and Bandyopadhyay, S., 2016. “Analytical determination of the proximity of two right-circular cylinders in space”. *Journal of Mechanisms and Robotics*, **8**(4), p. 041010.
- [46] Moore, M., and Wilhelms, J., 1988. “Collision detection and response for computer animation”. In *ACM Siggraph Computer Graphics*, Vol. 22, ACM, pp. 289–298.
- [47] Wellmann, C., Lillie, C., and Wriggers, P., 2008. “A contact detection algorithm for superellipsoids based on the common-normal concept”. *Engineering Computations*, **25**(5), pp. 432–442.
- [48] Barbagli, F., Frisoli, A., Salisbury, K., and Bergamasco, M., 2004. “Simulating human fingers: a soft finger proxy model and algorithm”. In *Haptic Interfaces for Virtual Environment and Teleoperator Systems, 2004. HAPTICS’04. Proceedings. 12th International Symposium on*, IEEE, pp. 9–17.
- [49] Howe, R. D., Kao, I., and Cutkosky, M. R., 1988. “The sliding of robot fingers under combined torsion and shear loading”. In *Robotics and Automation, 1988. Proceedings.*, 1988 IEEE International Conference on, IEEE, pp. 103–105.
- [50] Strang, G., 1993. *Introduction to Linear Algebra*, Vol. 3. Wellesley-Cambridge Press Wellesley, MA.
- [51] MATLAB, 2015. *version 8.5.0.197613 (R2015a)*. The MathWorks Inc., Natick, Massachusetts.
- [52] Polhemus-Liberty. Polhemus-liberty wired electromagnetic position and orientation tracker. <http://polhemus.com/motion-tracking/all-trackers/liberty>. Accessed: 2017-04-22.
- [53] Darbon, J., Cunha, A., Chan, T. F., Osher, S., and Jensen, G. J., 2008. “Fast nonlocal filtering applied to electron cryomicroscopy”. In *Biomedical Imaging: From Nano to Macro, 2008. ISBI 2008. 5th IEEE International Symposium on*, IEEE, pp. 1331–1334.

- [54] Tracey, B. H., and Miller, E. L., 2012. “Nonlocal means denoising of ecg signals”. *IEEE Transactions on Biomedical Engineering*, **59**(9), pp. 2383–2386.
- [55] White, R. M., 1980. Comparative anthropometry of the hand. Tech. rep., DTIC Document.
- [56] Manning, J. T., 2012. “Sex differences and age changes in digit ratios: Implications for the use of digit ratios in medicine and biology”. In *Handbook of Anthropometry*. Springer, pp. 841–851.
- [57] Arora, J., 2004. *Introduction to Optimum Design, Chapter 4, pp 154-157*. Academic Press.